Preprint statement: *This is a non-peer reviewed preprint submitted to EarthArXiv. The paper was submitted to Science of the Total Environment 12 July 2024 and is currently under review. New versions of the preprint might contain different content.*

More biomass burning aerosol is being advected westward over the southern tropical Atlantic since 2003

Tyler Tatro[1] and Paquita Zuidema[1]

[1] Rosenstiel School of Marine, Atmospheric, and Earth Science, University of Miami, Miami, FL, USA.

Corresponding author: Tyler Tatro (tyler.tatro@miami.edu)

Highlights:

- Burned area datasets indicate less fires in May but more in August and September.
- Smoke is carried further over the southeast Atlantic due to increased easterlies.
- Faster winds result from surface heating (thermal wind) and midlatitude changes.
- Increased warm temperature advection also helps maintain stratocumulus cloudiness.

Abstract

Each year, agricultural fires in southern continental Africa emit approximately one third of the world's biomass burning aerosol. This is advected westward by the prevailing circulation winds over a subtropical stratocumulus cloud deck. The radiative effects from the aerosol and aerosol-cloud interactions impact regional circulations and hydrology. Here we examine how concurrent changes in the burning season and regional climate in southern Africa over the past 18 years (2003-2020) impact the southeast Atlantic. We combine satellite-derived burned area datasets with ECMWF-reanalysis carbon monoxide, black carbon, and meteorology from the biomass burning season (May-October) in southern Africa. The burning season begins in May in woody savannas in the northwest and shifts to open savanna and grassland fires in the southeast, with small fires (less than 1 km^2) contributing significantly to total burned area. In the most recent decade, more small fires are occurring in the middle of the biomass burning season and the overall season is shorter, corroborated by reanalysis carbon monoxide fields. Significantly increased free tropospheric winds, shifted southward, transport smoke aerosol further southwest over the southeast Atlantic. The increased aerosol advection is coupled with a southern shift in the south Atlantic subtropical high and an increase in the low cloud fraction on the southern edge of the stratocumulus cloud deck. While smoke emissions sources have not changed significantly, changes in the smoke transport pathway, attributed to increasing surface temperatures in southern Africa and tropical expansion, combined with an altered low cloud distribution, explain how the regional radiation balance has shifted to more top-of-atmosphere cooling over the southeast Atlantic in recent decades.

Graphical Abstract

See Attached File

Keywords

Biomass burning; CAMS reanalysis; southern African easterly jet; tropical expansion.

1 Introduction

Southern continental Africa contains approximately 36% of the world's burned area (Giglio et al., 2018) and emits approximately 30% of the world's biomass-burning (BB) aerosol (smoke) and black carbon (Van Der Werf et al., 2010). The smoke is advected west from May through November, residing both below and above the subtropical southern Atlantic stratocumulus cloud deck (Adebiyi & Zuidema, 2016; J. Zhang & Zuidema, 2021). This is one of the major low cloud decks on the planet (Klein & Hartmann, 1993) with the deck's ability to radiatively cool the global climate motivating many other studies of the southern Atlantic independent of the aerosol's influence (Bellomo et al., 2015; Seethala et al., 2015; Zuidema et al., 2016; Scott et al., 2020). The radiative impact of just the smoke-cloud interactions has also become appreciated more over the past decade. When the smoke is located above the low clouds, the smoke absorbs incoming shortwave radiation and strengthens the cloud-capping inversion, ultimately increasing low cloud cover and 'cooling' the earth's surface (Adebiyi & Zuidema, 2018; Gordon et al., 2018; Herbert et al., 2020). Smoke entrained into the boundary layer can support both aerosol-cloud microphysical interactions (Twomey, 1977; Kacarab et al., 2020; Zhang & Feingold, 2023) and cause a cloud 'burn-off' (semi-direct effect) (Hansen et al., 1997; Ackerman et al., 2000; Zhang & Zuidema, 2019) by increasing stability in the boundary layer, decoupling the cloud layer from surface moisture sources (Johnson et al., 2004; Abel et al., 2020).

Many of the more recent studies documenting these interactions of the advected smoke with the stratocumulus deck have benefitted from the focus provided by recent field campaigns in the southeast Atlantic: the NASA ObseRvations of Aerosols above CLouds and their intEractionS (ORACLES) campaign (Redemann et al., 2021), the U.K. Cloud-Aerosol-Radiation Interaction and Forcing: Year 2017 (CLARIFY) campaign (Haywood et al., 2021), the French-led Aerosol Radiation and Clouds in southern Africa campaign (AEROCLO-Sa) campaign (Formenti et al., 2019), the European Dynamics–Aerosol–Chemistry–Cloud Interactions in West Africa (DACCIWA) project

(Denjean et al., 2020) and the Department of Energy Layered Atlantic Smoke Interactions with Clouds (LASIC) field campaign (Zuidema et al., 2018). Major findings include that the smoke is more abundant in the remote marine boundary layer and more absorbing of sunlight per particle and hygroscopic than previously thought (Zuidema et al., 2018; Kacarab et al., 2020; Wu et al., 2020; Dedrick et al., 2024), and that the aerosol needs to be just above the low cloud deck for the semi-direct stabilization of the free troposphere to be effective (Herbert et al., 2020). In addition, the smoke is more spatially and vertically extensive than had been previously appreciated (Das et al., 2017; Rajapakshe et al., 2017; Barkley et al., 2019; Holanda et al., 2020; Shinozuka et al., 2020; Doherty et al., 2022) . These findings increase the range of potential aerosol-cloud interactions contributing to the overall net radiative impact of the BB emissions. Increased cloud droplet number concentrations (N_d) from smoke intrusions into the cloudy boundary layer have been shown to increase cloud brightness and lengthen cloud lifetimes by suppressing precipitation (Christensen et al., 2020), and to promote cloud breakup through enhanced entrainment-evaporation (Zhang and Feingold, 2023).

At the same time, other studies highlight that BB aerosol-cloud interactions are difficult to depict realistically within models ranging from eddy-resolving to global climate (Brown et al., 2021; Mallet et al., 2021; Baró Pérez et al., 2024), in part because the large-scale circulation is likely also affected by the smoke (Johnson et al., 2004; Adebiyi & Zuidema, 2016; Das et al., 2020; Diamond et al., 2022; Johnson & Haywood, 2023), which introduces additional model variability. Overall, the complexity of the contributing processes helps explain why a lack of consensus remains on which aerosol-cloud interaction processes are dominant, and why such consensus may not be quickly forth-coming, despite ongoing improvements in model representations (Lou et al., 2020; Zhong et al., 2023).

A positive outcome, however, is that the new datasets are confirming that relatively new aerosol reanalyses are capturing realistic synoptic variations in BB aerosol (Pistone et al, 2024), as will also be shown here. In addition, the ability of satellite datasets to represent aerosol optical depth (AOD), and low cloud properties central to identifying the aerosol impacts - are also becoming better understood and appreciated (Grosvenor et al., 2018; Gryspeerdt et al. 2022; Arola et al., 2022). Such datasets are becoming more valuable as they continue to extend in time for evaluating recent trends relevant to climate change and aerosol-cloud interactions.

In an example relevant to this study, Jouan and Myrhe (2024) (JM24) report a detectable increase in the amount of BB aerosol over the southeast Atlantic in the past two decades using AOD as a smoke indicator, also documented in (Mehta et al., 2018; Kramer et al., 2021; Gupta et al., 2022). JM24 also find a net positive all-sky direct aerosol

radiative effect, indicating that shortwave absorption by aerosols in cloudy-sky regions is dominating the net response. The study reports mostly statistically insignificant reductions in liquid water path (LWP) and cloud fraction (CF) (changes in N_d are not considered). This implies that changes in the direct aerosol radiative effect (DARE) dominates the overall net radiative effect from aerosols, at least for the past two decades.

The root cause to the increase in AOD over the Atlantic Ocean remains an open question, however, as does an explanation of the cloud property changes (or lack thereof). The search for the underlying processes is the objective of this paper as. To do so, we also consult global fire emissions burned area datasets, and primarily rely on carbon monoxide (CO) as depicted within the CAMS reanalysis (Inness et al., 2019) as our proxy for smoke transport. Here, we compare the recent trends in fire distribution, meteorology, and cloud response over southern continental Africa (SHAF, defined as 0-35°SHAF) and the southeast Atlantic, during May through October for the period 2003-2020. Meteorological reanalysis extends further back and allows us to contextualize recent fire trends with 40-year trends (1980-2020) in reanalysis winds, humidity, and temperature.

2 Data and Methods

We focus on May through October and exclude November because the average burned area is ~4 times less in November than in May (both are transition months) and because no November temporal trend in burned area is apparent (Sections 3.0 and 4.1). Aerosol reanalysis is limited from 2003 onward as data from the *Aqua* and *Terra* satellites are assimilated after 2002.

2.1 Burned Area Data

We use burned area as our indicator of fire trends since burned area provides a consistent, first-order constraint on changes in fire dynamics (Andela et al., 2017). Both burned area and fire radiative power (FRP) reveal insights into burning conditions, but burned area detection is generally less subject to satellite overpass time; burned landscapes remain detectable for multiple days after the fires are extinguished (with the exception of croplands (Hall et al., 2021)). In contrast, FRP observations require real-time detection of active fires and are more subject to cloud obscuration errors over Africa (Boschetti et al., 2019). Overall, these concerns mean fire trends based on burned area estimates are less noisy than those based on FRP. Emissions datasets are a useful alternative, but current datasets still differ by as large as a factor of 4 in organic carbon emissions from southern Africa (Pan et al., 2020) and lack

agreement on the amount of CO produced (Griffin et al., 2024). Conventional passive satellite-derived AOD data does not provide information on aerosol vertical structure, importantly whether the smoke is above or within the boundary layer. The AOD retrievals are limited to clear-skies, an issue for the perennially cloudy southeast Atlantic. The clear-sky retrievals remain subject to cloud influences (Wen et al., 2007) and must be extrapolated either in space or time to also apply to cloudy skies, calling their representativeness into question (Schutgens et al., 2017; Shinozuka, Kacenelenbogen, et al., 2020).

Since recent burned area estimates have demonstrated that small fires previously missed by MODIS (see Appendix A) contribute significantly to total burned area (Roteta et al., 2019; Ramo et al., 2021), we compare two recently-produced fire datasets that account for the small fires as baselines for constraining the source emissions of biomass burning aerosol. The FireCCI51 data product (Lizundia-Loiola et al., 2020), developed by the European Space Agency's Climate Change Initiative Program, uses an additional near-infrared channel within MODIS and an alternative cluster-based thresholding algorithm to capture more of the small fires than do other MODIS-derived products (for July and September 2016), but ultimately FireCCI51 uses MODIS 250-meter data to calculate burned area. The other dataset, the Global Fire Emissions Database version 5 (GFED5, Chen et al., 2023) combines MODIS with higher-resolution Landsat and Sentinel 2 burned area datasets to apply historical corrections to account for previously missed small fires. Both datasets are the most recent burned area products available for 2003 to 2020, with both detecting more fires over southern Africa than the standard MODIS product (MCD64A1).

Both datasets are available on a 0.25°x0.25° grid but use different underlying land classification systems. We use both products to contextualize recent trends. The GFED5 product incorporates multiple external datasets to verify burned area values and calibrate scaling coefficients for small fires and, and we rely on it to examine monthly changes in burned area by land cover class. The GFED5 land classes are based on a modified International Geosphere-Biosphere Program classification (Figure S1) following Table S1 in Van Wees et al., (2022). The comparison of the GFED5 and FireCCI51 data products is one way to account for the uncertainty of accounting for small fires.

2.2 Aerosol and Gas Data

We use monthly-averaged carbon monoxide (CO) and black carbon (BC) fields from the ECMWF's Atmospheric Composition Reanalysis 4 (CAMS, Inness et al., 2019) to investigate smoke trends. CO has a relative atmospheric

lifetime of weeks to months (Holloway et al., 2000). CO emission trends from BB are masked by global and local anthropogenic trends from industrial centers but are better constrained by data assimilation than is BC, which has a shorter lifetime due to wet deposition. Western Africa has experienced a large population growth centered near the Gulf of Guinea (Moriconi-Ebrard et al., 2016), but biomass burning remains the largest source of total CO emissions from June to October in southern hemisphere Africa (Liousse et al., 2014).

A comparison of ORACLES flight data to the Modern-Era Retrospective Analysis for Research and Applications version 2 (MERRA-2) reanalysis (Gelaro et al., 2017) and the CAMS reanalysis by (Pistone et al., 2024) showed that CAMS specific humidity and CO correlate substantially better with observations than do the MERRA-2 fields. CAMS CO fields are provided at a 0.75x0.75° spatial resolution, with 25 vertical levels (7 levels between 1000 and 500 hPa). BB emissions in CAMS are driven by the Global Fire Assimilation System (GFAS) version 1.2 (Kaiser et al., 2012), which typically produces lower CO emissions than other datasets (Wiedinmyer et al., 2023). Version 6 total column CO retrievals derived from the thermal infrared band of the Measurement of the Pollution in the Troposphere (MOPITT v.6) instrument are also assimilated into the CAMS reanalysis. CAMS concentrations of CO compare well to satellite and aircraft values over long trajectories (Johansson et al., 2022; Ceamanos et al., 2023) and over seasonal and diurnal variations in black carbon and CO at select locations (Ding & Liu, 2022). CAMS CO values at 960 hPa in the remote boundary layer match the variability of LASIC observations at Ascension Island at 8°S, 14.5°W well (explained variance of 0.64 and 0.60, for June-October 2016 and 2017, respectively, (Fig. A1).

The MOPITT weighting function is more sensitive to upper-altitude CO (300-700 hPa) than lower levels over both oceans (Deeter et al., 2003) and over tropical African rainforests (Deeter et al., 2007), therefore, we reduce the uncertainty in CAMS CO introduced by the data assimilation by separately integrating mid-tropospheric CO (500-700 hPa) and lower tropospheric CO (700 to 1000 hPa) to analyze smoke located above the cloud (carried by free tropospheric winds) or smoke collocated with the cloud. The distinction also allows us to examine changes in the BB loading above and within the cloudy boundary layer separately. We define these quantities as

$$(1)\ CO_{MT} = -\int_{700\ hPa}^{500\ hPa} CO_i dp$$

$$(2)\ CO_{LT} = -\int_{1000\ hPa}^{700\ hPa} CO_i dp$$

where CO_i represents the mass fraction of CO. After removing a background global reduction in CO (see Appendix A2), we process this data following the methods in 2.4. We similarly analyze black carbon (BC) from CAMS, taken as the sum of the hydrophilic and hydrophobic black carbon mass tracers. The CAMS BC also correlates well to BC observations at Ascension Island (explained variance of 0.55 and 0.65, for June-October of 2016 and June-August 2017, respectively). The slight underestimate in CO and overestimate in BC concentrations suggests remaining errors in the underlying emission factors, but this error source will not impact trend estimates.

2.3 Meteorological and Cloud Data

We examine for meteorological changes in cloud-controlling factors using sea surface temperature (SST), estimated inversion strength (EIS;Wood & Bretherton, 2006) and surface-level, cold air advection (Seethala et al., 2015; Adebiyi et al., 2015; Scott et al., 2020) as well as in wind, temperature and humidity patterns, and in cloud property changes potentially induced by aerosol. Monthly-mean low cloud fraction and low cloud liquid water path, at a one-degree spatial resolution, come from the Clouds and the Earth's Radiant Energy System (CERES) CldTypHist_Ed4A product (1x1°) (Wielicki et al., 1996). The data product combines Terra-MODIS and Aqua-MODIS retrievals based on the CERES SYN1deg Ed4A retrievals (Winker et al., 2009). Low clouds possess cloud top pressures greater than 680 hPa and any optical depth greater than 0, meaning partly-cloudy pixels are also included in the cloud fraction. Daily N_d relies on the MODIS collection 6.1 cloud optical properties retrieval dataset (MOD06_L2) for both the Aqua and Terra satellites (Platnick et al., 2017). We use the N_d dataset constructed using the selection criteria detailed in Grosvenor et al., (2018) and Gryspeerdt et al., (2022). The N_d retrievals are restricted to the more optically-thick and horizontally homogeneous clouds less subject to retrieval artifacts, detailed further in Appendix A3. Monthly-averaged meteorology (winds, temperature, humidity) and sea surface temperature are established by ECMWF's Reanalysis 5 (ERA5, 0.25x0.25°) over 1980 to 2020 (Hersbach et al., 2020).

2.4 Methods

We calculate monthly anomalies before computing the least-squares regression slope for each parameter and compare them independently to trends in other data. Datasets differ in spatial resolution, but since this analysis

is focused on spatially coherent, long-term trends computed with monthly data on scales greater than grid size, a qualitative comparison of the trends between datasets (as opposed to a multiple linear regression model) is deemed sufficient. The standard error of the estimated slope is provided as are p-values calculated using a Wald Test with a t-distribution (two sided).

3.0 Seasonal Overview

The fires over Southern Africa are primarily small and human-initiated, intended to prepare land for grazing through burning grasses, leaving fire-adapted trees intact, and to a lesser extent burn previously slashed trees (van Wilgen et al., 1990). A clear diurnal cycle, with more burning occurring during the day (Giglio et al., 2006; Roberts et al., 2009) facilitates the detection of burned areas using satellite visible imagery (Giglio et al., 2003). Fires begin in May in northern Angola and in the Democratic Republic of Congo (DRC) and move southeast through the end of October (Fig. 1a), which generally follows the drying pattern of the vegetation (Korontzi, 2005). Over 98% of the annual burned area in southern Africa occurs between May 1 to October 30, peaking in July-August (Fig. 1b), with 48% of the annual total burned from August 1 through October 31 in both GFED5 and FireCCI51 datasets. Since this period coincides with the dry season (Fig. 1c), the semiarid regions further south (10-20°S) are affected by interannual variations in rainfall; wetter years tend to increase fuel availability and burned area during the following burning season (Anyamba et al., 2003).

The annual cycle in total burned area leads that in column CO by one month, so that the peak in burned area occurs in August, while the peak in average total column CO occurs in September (Fig. 1b), averaged over the southern African continent. The total column BC is similar in August and September, despite the reduction in burned area. The seasonal cycle in burning conditions changes the ratio of CO within BB emissions. Fires at the beginning of the season burn less efficiently than peak season fires, since they consume forested areas with more saturated vegetation and woodier materials (Korontzi, 2005, Dobracki et al., 2024). As the season continues into July and August, fires burn a higher percentage of dry grasses. These undergo more complete combustion and result in a peak in burning efficiency as measured by FRP (Zheng et al., 2018) and the modified combustion efficiency, defined as the ratio of CO_2 to the sum of CO_2 and CO (Ward et al., 1996). One explanation may be a shift from flaming to more smoldering fires in September-October, when more of the dry grassy fuel is already consumed, leaving woodier materials to burn (Van Der Werf et al., 2006), combined with the return of rainfall (Fig. 1c).

Another explanation is that the long chemical lifetime of CO and increased transport from other biomass burning regions delay and shift the peak in CO concentrations to September (van der Velde et al., 2024).

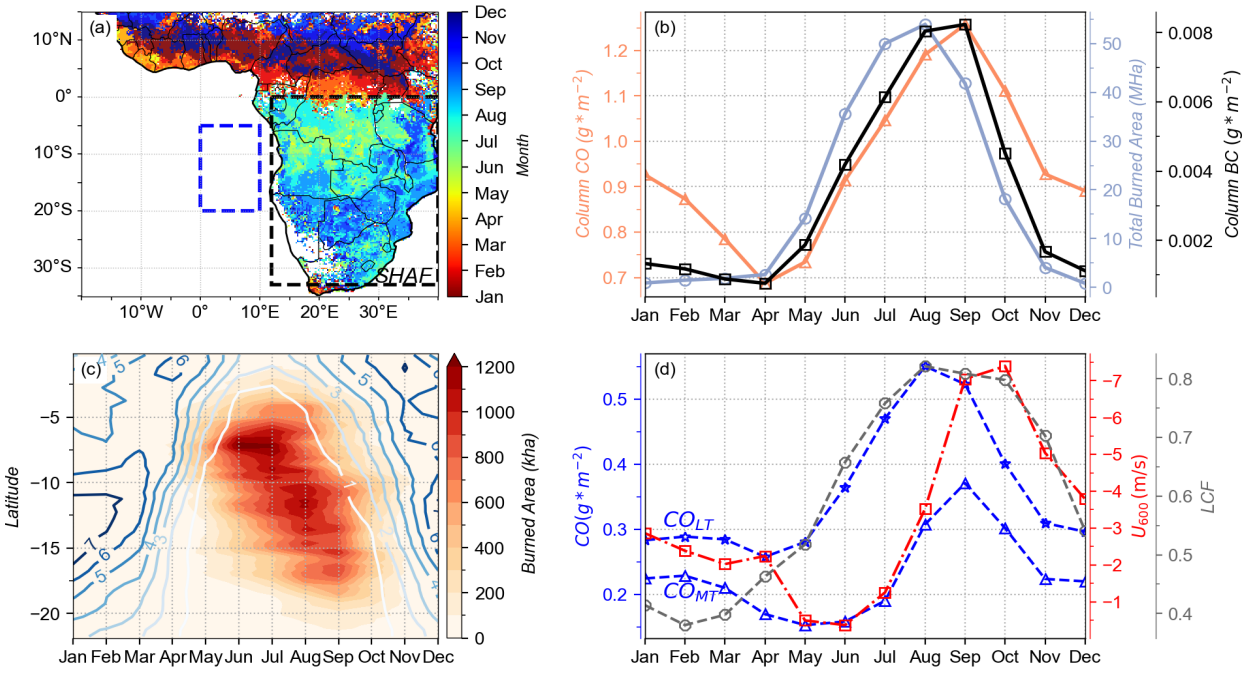

Figure 1. Seasonal cycle of **(a)** month of maximum in GFED5 burned area, **(b)** CAMS total column CO (orange line) averaged over SHAF (12^0E-40^0E, 32^0S-0^0 outlined in black dashes) and GFED5 total burned area (blue line) summed over SHAF, **(c)** GFED5 burned area (colored contour) and global precipitation climatology project precipitation (blue lines, 1mm*day^{-1} contours) averaged over 12-40°E and **(d)** CAMS column CO between 500 and 700 hPa (blue triangles) and between 700 and 1000 hPa (blue stars), ERA5 zonal wind at 600 hPa (red squares), and CERES low cloud fraction (gray circles) averaged offshore (5-15°S, 0-10°E, blue box in panel a).

Another aspect to the seasonal cycle, important for aerosol-cloud interactions, is the change in aerosol vertical structure. In June-July, most of the BB emissions over the southeast Atlantic ocean are located in the lower troposphere, at pressures > 700 hPa (Fig. 1d), with more of the aerosol located at higher altitudes beginning in August. In combination with the August maximum in burned area, this places most of the BB aerosol within the boundary layer at Ascension in August (Fig. A1). The change in aerosol vertical structure reflects changes in the large-scale meteorology. In June-July, much of the westward transport of aerosol is by slow, low-altitude easterlies encouraged by fortuitous placement of the south Atlantic sea level pressure high (Sun et al., 2017; Dobracki et al., 2024, Preprint). As the southern African continent warms in the austral spring, a dry heat low sets up in Angola

beginning in August, overlain by a mid-tropospheric high and separated from the moist Congo by a dryline (Attwood et al., 2024). The mid-tropospheric meridional surface temperature gradient between and above the moist Congo and the hot, dry Angolan plateau causes a thermal wind balance response. This response creates an annual maximum in mid-tropospheric easterlies (Fig. 1d), known as the Southern African Easterly Jet (AEJ-S; Nicholson & Grist, 2003; Adebiyi & Zuidema, 2016), defined as a monthly easterly windspeed exceeding 6 $m*s^{-1}$ between 5 and 15°S (Fig. 1d). As the land heating intensifies and moves to the Kalahari plateau in September-October, the jet core also moves south and increases in altitude from 700 hPa in August to 600 between 700 and 500 hPa (Ryoo et al., 2021). The strong easterlies combine with the fire emissions to transport smoke westward at higher altitudes in August-October (Redemann et al., 2021), with synoptic modification from, e.g., mid-latitude disturbances (Kuete et al., 2020).

The stratocumulus cloud deck is largest between July through September (Fig. 1d, Ryoo et al., 2021). In July and August, higher smoke concentrations within the boundary layer increase N_d (Fig. A3), alter the near-surface radiative heating profile and decrease low cloud fraction near Ascension Island (Zhang & Zuidema, 2019; 2021). In September and October, the higher altitude of BB aerosol can promote low cloud fraction by stabilizing the lower troposphere through absorbing incoming shortwave radiation (Wilcox 2010; Adebiyi et al., 2015; Adebiyi & Zuidema, 2018).

4 Results

4.1 Steady Continental Emissions but a Changing Fire Seasonality

Most of the fires in southern Africa occur in open savannas during May-October months (Figs. 2-3), followed by tropical grasslands and woody savannas, with tropical forests burning the least until later in the season and in recent years. Burned area within the first half of the BB season (Figure 2) is comprised of fires in open savannas (Fig. S1) near the southern edge of the rainforest in the DRC and in the north of Angola. May shows a significant total decrease in burned area (-0.36 Mha ±0.149 or -2.5% of the monthly mean per year) with fires decreasing in tropical forests, woody savannas, and open savannas (Fig. 2a). The gradual decrease in May is centered near the northern Angola-DRC border (Fig. 2b) in the Lunda Norte and Malanje provinces (Catarino et al.,

2020), and in the Kasai province of the DRC. Both June and July show significantly less fires in woody savannas, and slightly increased burned area in open savannas, which combine for a negative but insignificant net burned area trend for both months (-0.027 ±0.154 and -0.083 Mha ±0.151 per year, respectively).

June shows increased burned area in the central DRC, slightly east of the areas decreasing in May, consistent with increased forest clearing rates for small-scale rotational agriculture (Tyukavina et al., 2018), and the negative correlation of burned area with population density in this location (Andela et al., 2017). The June increases also mirror the trends found by Wimberly et al., (2024), indicating strong correlations of burned area with maximum temperature and vapor pressure deficit at this location. The increases may come about from a combination of less local rainfall (Zhou et al., 2014) and population changes in the wake of internal displacement from conflict (UNHCR, 2023). The latter are likely fragmenting the landscape, since less of the forest loss is associated with fire over time (van Wees et al., 2021). This reduces fire size and shifts the locations of burning, causing a significant reduction in May and increase in June. Significant decreases in July are concentrated in northeastern Tanzania near game reserves, which we speculate reflects forestry management practices (Ract et al., 2024).

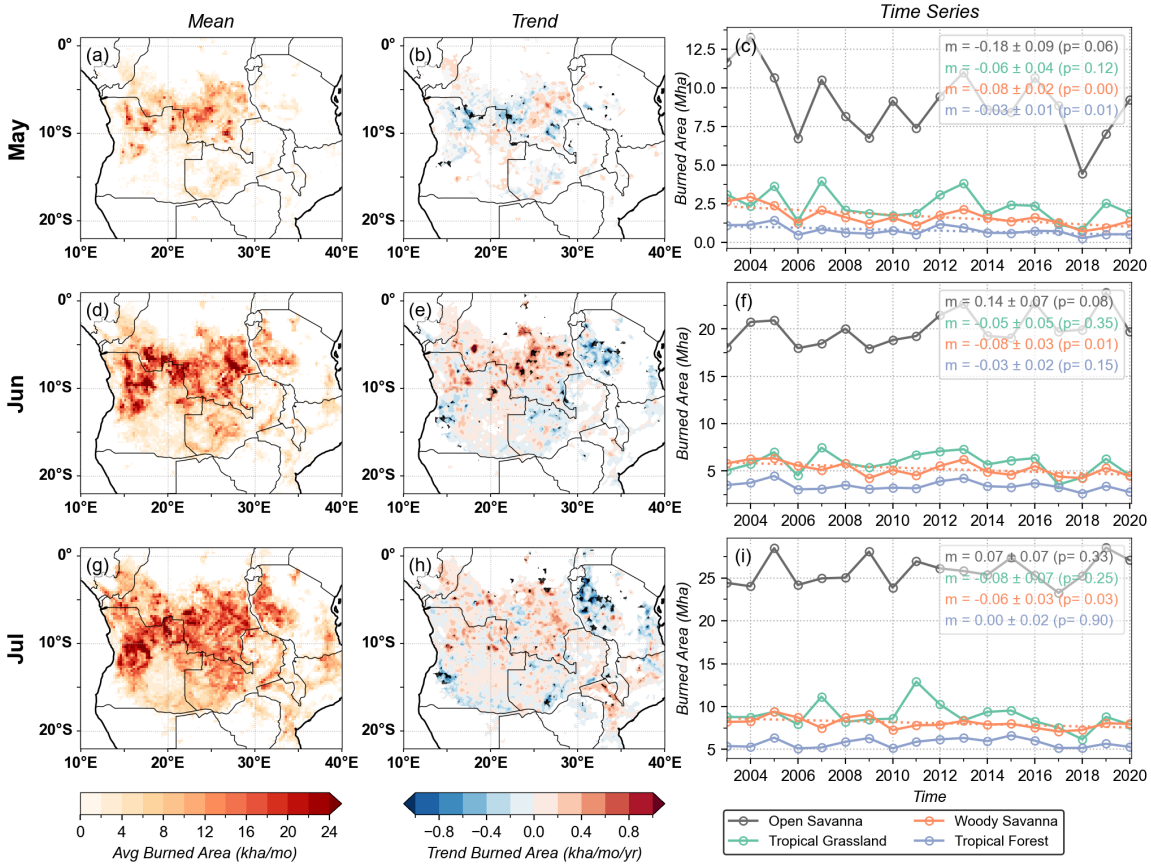

Figure 2. Spatial plots of mean burned area **(a,d,g)**, trends (**b,e,h**), and linear time series of burned area **(c,f,i)** by vegetation class for May-July from 2004 to 2020 for the SHAF box shown in Fig. 1. The y-axis range in panels c, f, and i differ. Black stippling on panels (b,e,h,) and time series with dashed linear fits indicate significant trends at the 95% confidence level.

In the second half of the season (Figure 3), the proportion of fires in tropical grasslands increases from August (20%) to October (26%) as the fires move southeast. In August, growth in savanna fires (0.19 ±0.082 Mha/year) slightly outpaces significant decreases in grassland fires (-0.13 ±0.045 Mha/year) and other classes, resulting in a near-zero net trend (.019 ±0.16 Mha /year). Fire_CCI shows the largest deviation from GFED5 burned area trends (Figure S2) in August (-0.47 ±0.22 Mha/year). Since GFED scales for small fires, this discrepancy can be understood as an increase in small fires in the month of August. Even though the detection of small fires should extend the traditional fire season (Ramo et al., 2021), August and September (0.12 ±0.21 Mha/year) are the only burning season months with net increasing (but insignificant) burned area trends in GFED5.

Both datasets show decreases in October, when the fires are concentrated in northeast Zambia and along the coast of Mozambique (Fig. 3e, h). Spatial maps of the monthly trends reveal that burned areas increase at these locations in September as well– suggesting that these locations are burning earlier. This may reflect a combination of both fire management practices encouraging earlier burns in the season, and human encroachment favoring deforestation for croplands (Phiri et al., 2023), but this explanation remains speculative. Overall, increased burning in September combined with decreased burning in October acts to amplify the seasonal cycle.

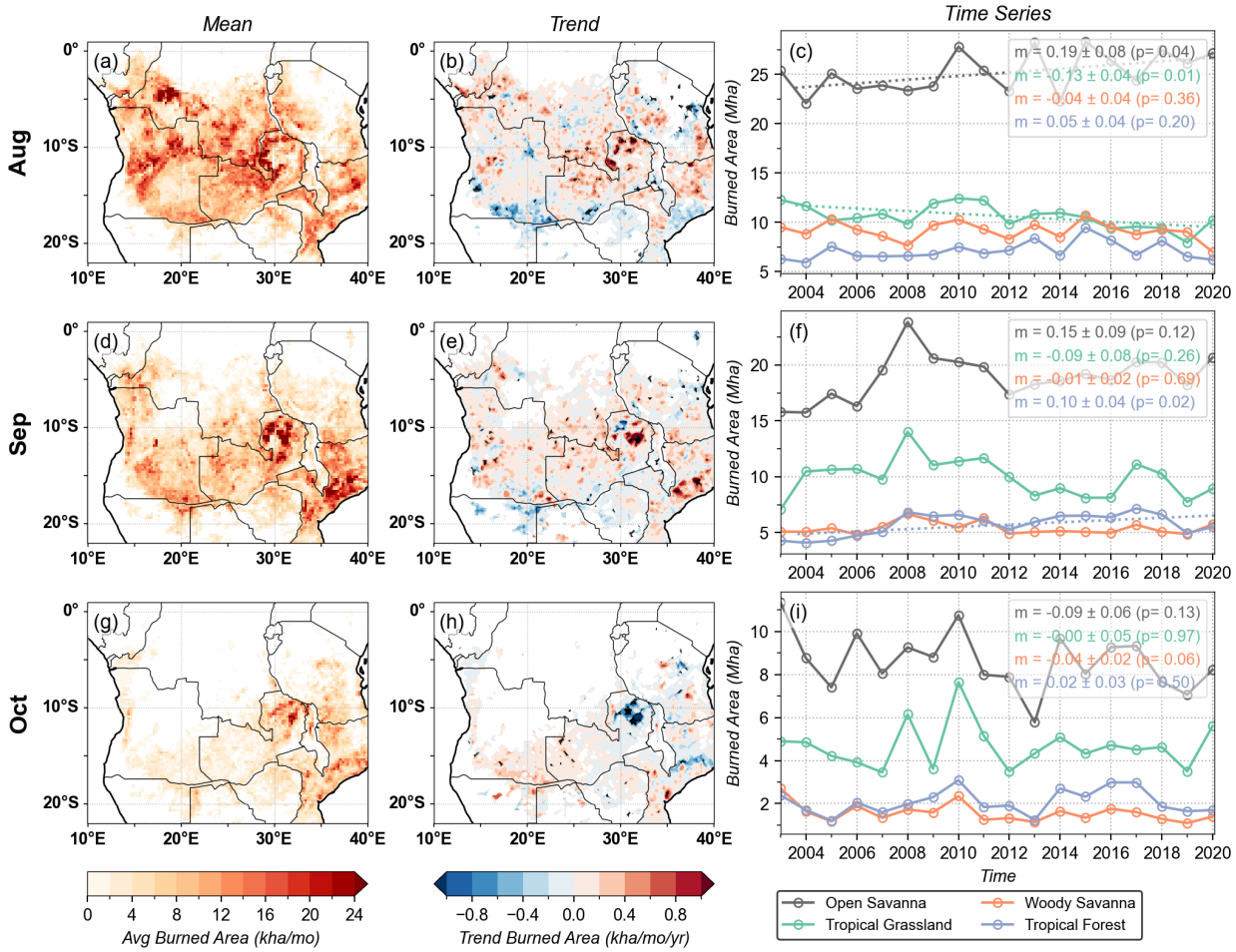

Figure 3. Same as Figure 2 but for August-October.

The decreases in burned area in May and October and increases in open savanna fires in August and September, compress the BB season in time, but with a more amplified 'peak', shifted to slightly later in the year (Figure 4a). CO and black carbon in the lower troposphere (the integral from the surface to 700 hPa; Figs 4b and c) corroborate the decline in burned area in May. The increase in CO from November-March is best explained by increased anthropogenic emissions (Liousse et al., 2014). In August near 11°S, there is a modest but insignificant uptick in black carbon (Fig. 4c), indicating GFAS may be detecting part of the increase in burned area. The lack of a CO signal in August and September could also stem from proportionally more dry grass fires that burn hotter, and proportionally emit less CO.

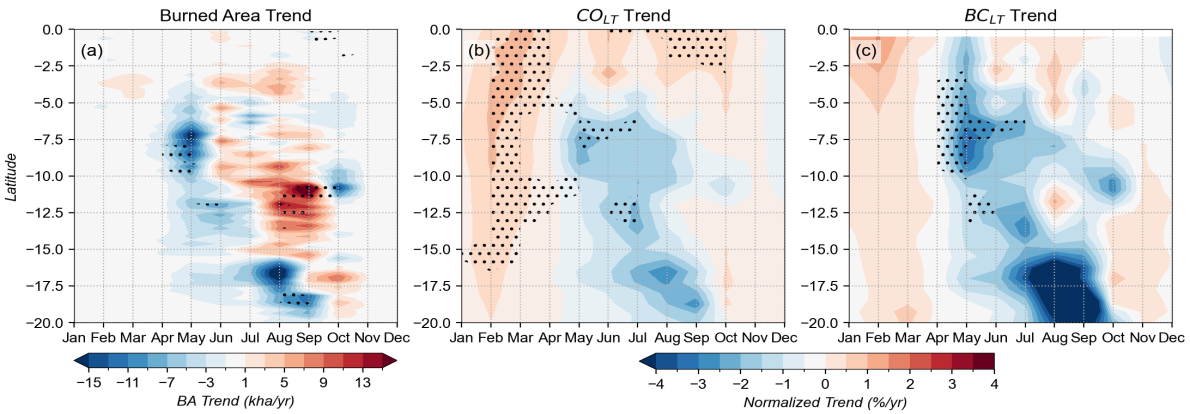

315

316 **Figure 4.** 2003-2020 trends in **(a)** GFEED5 burned area**, (b)** residual CO in the lower troposphere, and **(c)** black
317 carbon in the lower troposphere. Black stippling significant trends at the 90% confidence level. Domain spans 12^0E-
318 40^0E.

319

320 Despite seasonal changes, the annual average GFED burned area and total column CO (Figure 5) are
321 approximately constant from year to year (coefficients of variation of 3.7% and 3.4%, respectively). The Fire_CCI
322 burned area estimate begins to decrease after 2011 for southern Africa (Fig. 5a), with a BB season trend of -1.62
323 ±0.41Mha per year (or 1.0% per year), which is slightly less than the decreases found by Jiang et al. (2020).
324 GFED5-estimated burned area is 40% higher than Fire_CCI estimates, and, importantly for this study, GFED does
325 not show a strong decrease in burned area after 2011 (total trend of -.44 ±0.38 Mha or -.20% per year). This
326 illustrates the uncertainty of accounting for small fires. Jiang et al (2020) find no trend for fires smaller than 100 ha,
327 but because GFED scales for small (and undetected) fires, then the difference between the two datasets must
328 primarily be because the number of small fires has been increasing since 2010.
329 The CAMS season-average total column CO and BC over SHAF correlate well with GFED5 (r=0.68 and
330 r=.78, respectively), and Fire_CCI (r=0.59 and r=.76, respectively) burned area, but lack the significant global
331 decrease shown by the global area average of column CO (Fig. 5b). Background CO concentrations during the
332 burning season over continental Africa are too high to be strongly affected by the global reduction, but we see
333 interannual values altered by global signals. An example is the peak in the extreme El Niño summer of 2015
334 associated with equatorial zonal transport from peat fires in Indonesia (Field et al., 2016) in both the local and global
335 signals. The global CO average reduces in 2008 as a consequence of the economic recession (Yurganov et al.,
336 2010) and never recovers, attributed to improvements in combustion technology and higher air quality standards.

Black carbon significantly decreases from 2012 to 2020 (-3.7 ±0.55% per year, p<.001), or a 25% reduction from the peak in 2012. Column CO was also a minimum in 2018, but CO's relative decline of 12% from 2015 is smaller. Given the reduction in burned area is not so pronounced, we suspect a combination of reasons for the decline.

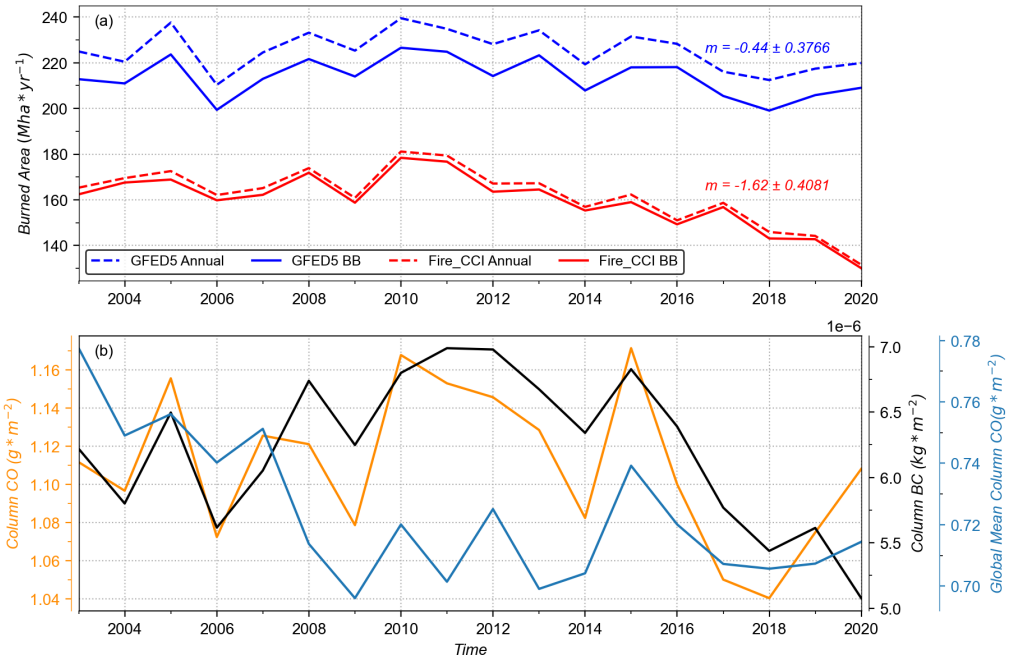

Figure 5. Time series of **(a)** Total burned area in the GFED5 dataset (blue line) and Fire_CCI dataset (red line) annually (solid lines) and between May-October (dashed lines), and **(b)** Regional and global column CO (orange and blue lines, respectively) and regional column black carbon. Regional domain of averaged between 0-30°S, 12-40°E.

4.2 Zonal Wind Increases in the Lower Free Troposphere

From May through July, the easterly 800 hPa winds at the west side of southern Africa indicate a small but robust increase over the 1980 to 2020 time span, concentrated over the tropical Atlantic ocean near coastal Angola (Fig. S3). Easterly winds during August to October have increased in both strength and width over the past 40 years (1980-2020; Figure 6 a,b,c) over the continent and the ocean. The increase in August AEJ-S winds is not significant (-0.002 m/s per year) but the latitude of the maximum wind speed does shift to the south (-0.026 ± .0075° per year, p <.005) (Figure S4). Average jet speeds increase in September (-0.04 ± .01 m/s per year) and October (-0.06 ± .01 m/s per year) (brown shading; Figure 6 d,e,f), concentrated near the mean jet location (pink contours). This also allows the jet latitudinal width to expand (.07 ±.03°/year, p <.05 and 0.11 ± .03°/year, p <.01 in September and

October, respectively). Increases in easterly wind speed are also more prominent above the mean jet altitude in August and September, although the altitude of maximum AEJ-S speed does not exhibit a detectable increase.

The increase in easterly wind is concentrated on the northern side of the shifting subtropical jet noted in Manney & Hegglin (2018) and Woollings et al., (2023). The westerlies associated with the storm tracks at 30°S have also increased in speed (green shading), thereby increasing the latitudinal gradient in zonal wind, more notably in September and October. The increase in temperature (red contours) near the mean location of the surface heat low (between 900 and 600 hPa and 15°S-25°S) is prominent in all three months and increases in relative strength from August (0.35%) to October (0.64%).

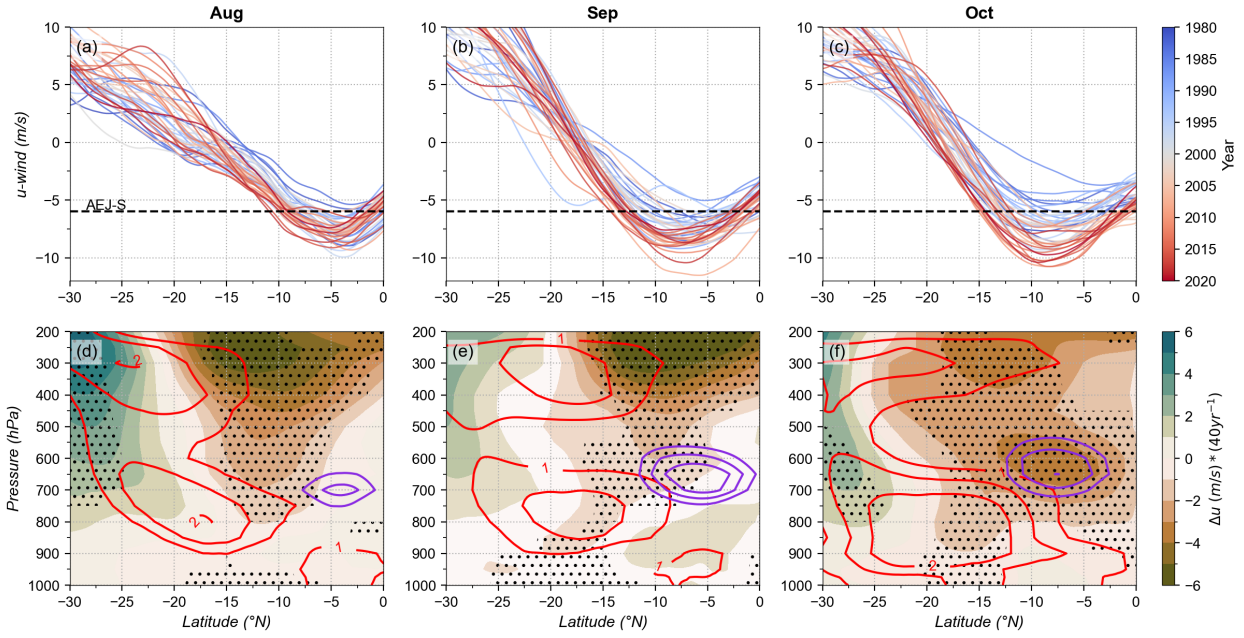

Figure 6. Top row: Monthly-mean u-wind profile at 700 hPa, 600 hPa, and 600 hPa color-coded by year for **(a)** August, **(b)** September, and **(c)** October, colorized by year, averaged over 0°-25°E. Bottom row: Height versus latitude 40-year trends in zonal velocity (u; shading) and 40-year trends in heating (red contours, 1,1.5,2 K) and the mean AEJ-S contours (purple, -6 to -8m/s) for 1980-2020 (bottom row), averaged over 0°-25°E. Stippling indicates significance of u-wind trend at the 95% confidence level.

The strengthening and southward shifting of the AEJ-S can be understood as the consequences of two separate long-term changes: a strengthening of the thermal wind through the warming of the southern African

continent, and a poleward expansion of the Hadley circulation that is preferentially supporting more warming towards the south. We consider the monthly mean thermal wind change by approximating the vertical wind shear as:

$$(3)\ U \simeq \frac{-R_D}{f} * \frac{\partial \langle T \rangle}{\partial y} \ln\left(\frac{p}{p_s}\right)$$

where U is the zonal wind at 600 hPa (700 hPa for August), R_D is the dry gas constant, f is the Coriolis parameter, $\langle T \rangle$ is the vertically averaged temperature, y is the latitude, p is the pressure at the jet level, and p_s is the pressure at the surface (1000 hPa). We assume the contribution from the surface wind is negligible for this exercise, so that the thermal wind magnitude is also equal to the wind approximated from geostrophic balance. The independently calculated trend in thermal wind captures the relative magnitude of the zonal wind change, despite overpredicting the ERA5 zonal wind trend over land and underpredicting it over the ocean (Figure 7) in all three months. Even though the correlation between jet intensity and the meridional surface temperature gradient increases from September to November (Kuete et al., 2023), September shows a stronger agreement over land than October. The spatial trends in temperature (Figure S5) reveal warming near the southern edge of the Congo Basin Rainforest during May-October and a larger heating signal concentrated between 15° to 20°S encompassing the Angolan plateau to the northern edge of the Kalahari Desert in August to October. The warming is consistent with increases in Angolan heat lows in September and October (Attwood et al., 2024), which would provide more ascent up to the altitude of the AEJ-S.

The thermal wind budget does not consider momentum contribution from other sources, such as the winds associated with the south Atlantic subtropical high. We attribute the difference between the idealized wind and observed trend to the neglect of other momentum fluxes that can affect the easterly wind – such as the poleward shift of the storm tracks (Lu et al., 2007) reducing intrusions from midlatitude disturbances (Kuete et al., 2020), or increased easterlies over the ocean connected to the movement of the south Atlantic subtropical high (Vizy & Cook, 2016). Since changes in the jet speed are larger over the ocean in each month and more significant in September ($p=0.04$) and October ($p=0.005$) than August ($p=0.26$) in both ERA5 and the thermal wind equation, we suspect the southward movement of the South Atlantic High and warmer land surface temperatures encourage stronger easterlies over the ocean at 700 hPa during these months.

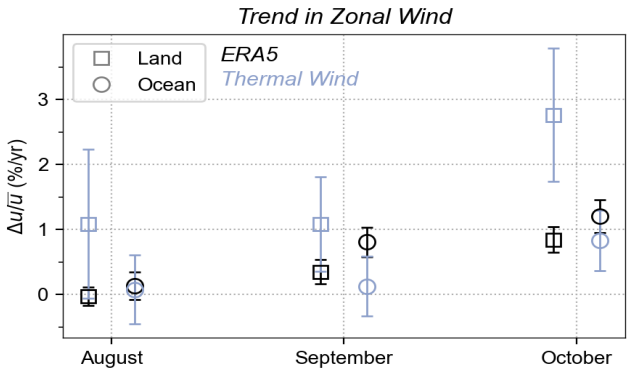

394

395 **Figure 7.** Monthly trends in jet speed between ERA5 (black) and thermal wind (Equation 3; gray) over land
396 (squares, 10-30°E and ocean (circles, -5-10°E) normalized by the monthly mean zonal wind in each region. The jet
397 region is defined as the 1980-2020 average domain in each month exceeding -6 m/s.

398 ## 4.3 Increasingly Smoky SEA Free Troposphere

399 Emissions of CO are decreasing in May over land, and increasing more in June-July, but trends in CO_{LT} and BC_{LT}
400 over the ocean are mostly insignificant, and when not, reflect the global CO reduction (Figs. S6-S7). Instead, the
401 main aerosol trend over the southeast Atlantic is from increased advection transporting more smoke into the free
402 troposphere above the ocean from August through October (Fig. 8, top row). Increases in BB aerosol during August
403 and September are most prominent over the stratocumulus cloud deck and shifted south of the mean location of the
404 AEJ-S, which we attribute to a southern shift in the mean location of the jet itself (section 3.2). Buchholz et al.
405 (2021) and Jouan & Myhre (2024) find similar increases in residual total-column CO and in AOD, respectively, in
406 the same location. Positive trends in CO_{LT} (Figure 8, bottom row) mirror trends in CO_{MT} for August to October (and
407 July, figure S6) but lack statistical significance in areas associated with biomass burning. All three months show
408 positive CO trends north of the equator from urbanization in western Africa. The increase of CO_{LT} in October (Fig.
409 8f) centered near 5°S corresponds to easterly wind speed increases that extend down to 800 hPa (Section 4.2), but
410 the source of the CO is likely due to urbanization since the fires are further southeast.

411 Positive residual trends in CO_{MT} in May through July (Figure S6) in Western Africa and south of 20°S are
412 linked to detrending the global CO reduction. A fraction of CO (between 0.2 to 0.6) over continental Africa in
413 August-October results from transport from other regions and long CO residence times (van der Velde et al., 2024).
414 However, a significantly increasing trend in BC_{LT} over the ocean in August (Figure S7d) in the same location as the

CO increase (Fig. 8d) confirms that more BB aerosol is likely present in the August marine boundary layer over time.

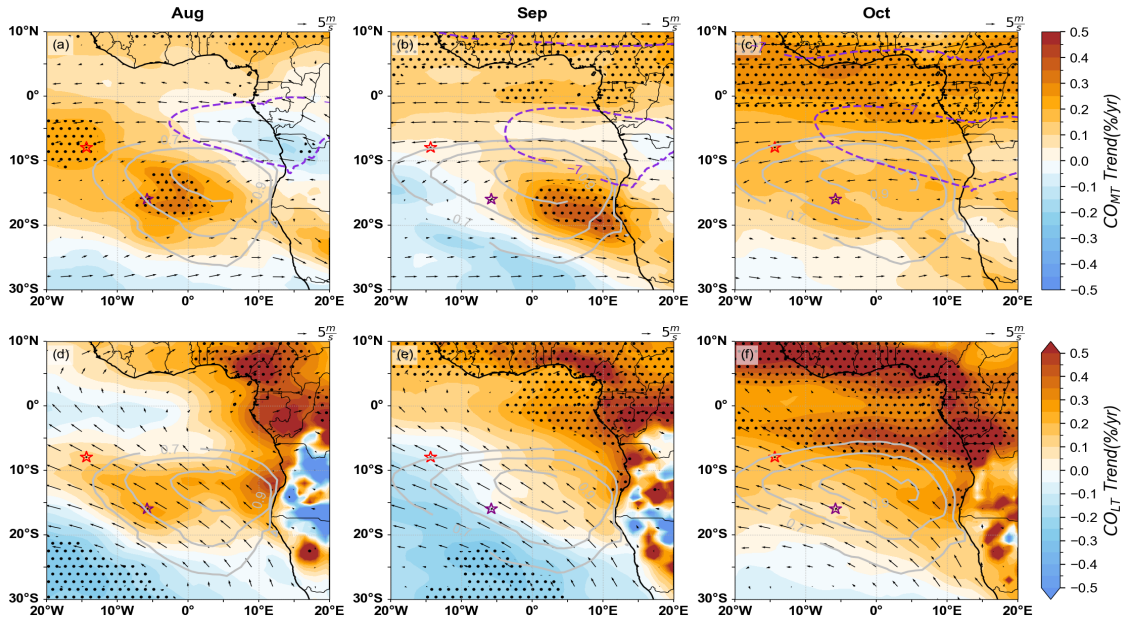

Figure 8. Residual trend in CO_{MT} (top row) for a) August, b) September, and c) October (shaded) expressed as a percentage of the CO column mean, shown with the mean jet locations (|u|>6,7,7 m*s^{1}, dashed pink contour), mean circulation at the AEJ-S (700, 600, 600 hPa) (vectors) and mean low cloud fraction (gray contours, 0.7-0.9) for 2003-2022 (a-c). Panels d-f indicate the residual trend CO_{LT} (bottom row) with the circulation at 900 hPa (vectors). Stippling indicates significance of the regression line at the 95% confidence level. Ascension and St. Helena islands indicated (light and dark red stars).

4.4 Impact on the Southeast Atlantic Stratocumulus Deck

The months when a trend in an aerosol-induced cloud response is most likely to occur are August and September, based on the analysis in Sections 4.2-4.3. N_d trends are shown along with those in CF, SST and EIS in Fig. 9 for August-October. A statistically-insignificant August increase in N_d (Fig. 9j) at the southwestern edge of the stratocumulus deck is nevertheless broadly consistent with an increase in CO and BC in that location. Cloud fraction is also decreasing in the same location, but the trend also lacks statistical significance.

In September, a stronger AEJ-S will increase warm temperature advection off of the continent (Adebiyi et al., 2015) as well as increase the offshore aerosol loading (Fig. 8b). A warmer free troposphere is apparent in a

statistically-significant EIS increase (Fig. 9h) coinciding with a (statistically-insignificant) cooler ocean (Fig. 9e). The September increase in lower tropospheric static stability should increase cloud fraction, but this is only apparent near the Namibian coast (Fig. 9b). Here, slight coastal SST cooling, likely associated with a southern shift to the coastal Benguela upwelling region stemming from increases in the near-surface wind at its southern end (Brandt et al., 2024), helps support cloud development. This includes cloud downwind supported through cold temperature advection (Fig. S8). Also noticeable is a statistically-significant decrease in cloud fraction in the northwest side of the stratocumulus deck (Fig. 9b) coinciding with a statistically-insignificant N_d decrease (Fig. 9j). Without further analysis we can only speculate on the responsible processes for these decreases. We note that in May-July, cloud fractions also mostly decrease basin-wide, with the exception of the coastal Benguela upwelling region (Fig. S9), suggesting an influence from increasing sea surface temperatures.

October is the only month with a statistically-significant (upward) N_d trend (Fig. 9l). The increase in N_d occurs broadly where EIS is also increasing (with statistical significance; Fig. 9i). Cloud fraction is also increasing and SST is cooling, though lacking in statistical significance (Fig. 9c,f). Given the lack of correspondence with a significant aerosol-related trend (Fig. 8c), the cloud changes are speculated to result from larger-scale circulation changes strengthening the southern edge of the stratocumulus deck, reducing Nd retrieval artifacts. The increase in cloud fraction at the southern edge of the stratocumulus deck is also captured by the JM24 analysis as well as Wall et al., (2023).

Liquid water paths (LWPs) increase over all three months (Figure S8), but insignificantly. The trend contradicts a slight LWP decrease documented by Jouan and Myrhe (2024) using more constrained sampling criteria. A LWP decrease is more consistent with the overall decrease in cloud fraction (Figs 9a-c). We hypothesize a retrieval artifact from the incorporation of ‘partly cloudy’ pixels in our LWP analysis that are excluded in the JM24 analysis. In summary, the strongest indicator of a statistically-significant trend with potential for aerosol-cloud interaction is an increase in lower tropospheric stability in September (Fig. 9b) that coincides with a statistically-

significant CO increase (Fig. 8b).

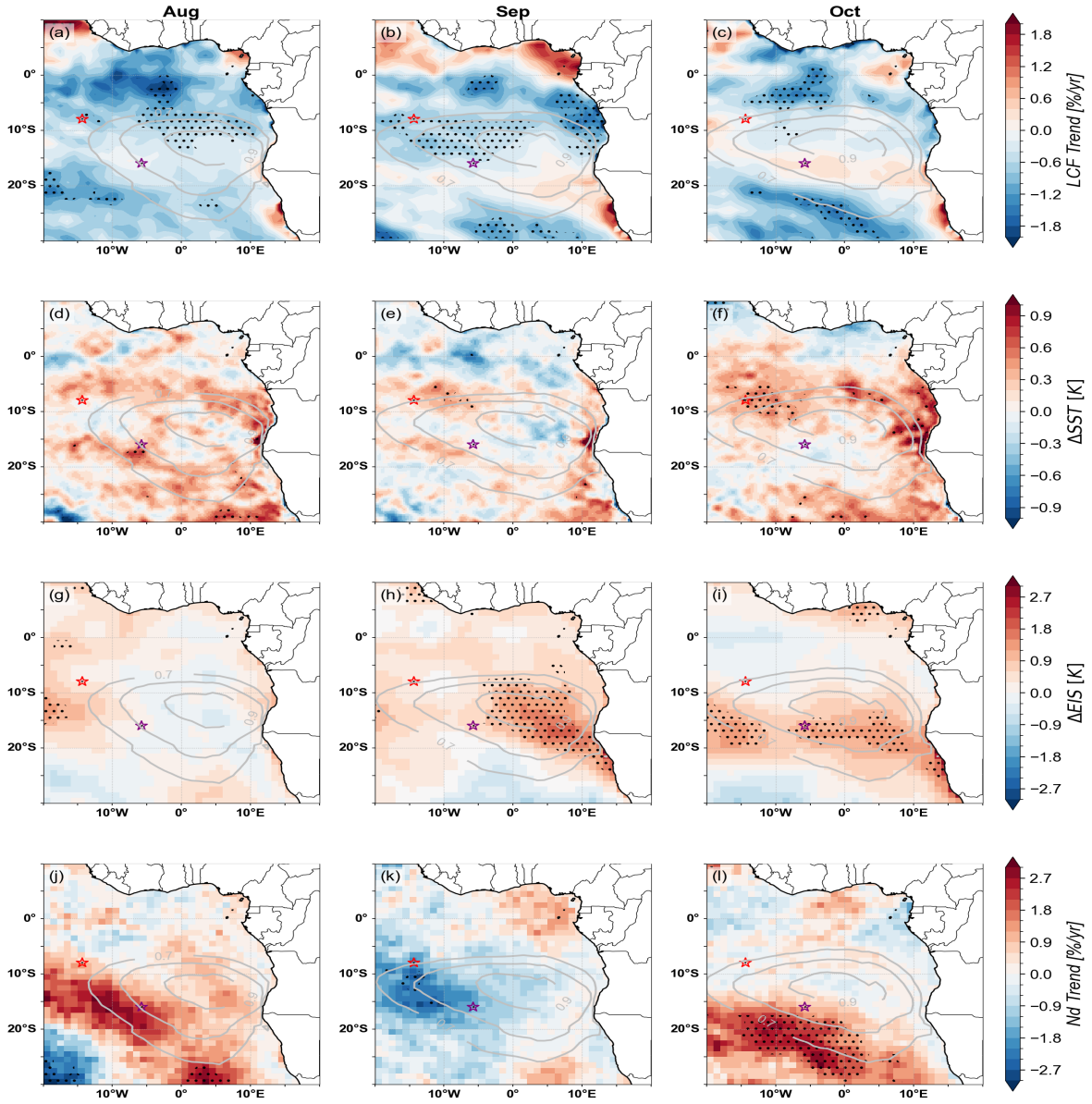

Figure 9. Recent trends (2003-2020) in CERES low cloud fraction (first row), ERA5 sea surface temperature (second row) CERES estimated inversion strength (third row), and MODIS cloud droplet number concentration (fourth row) for August (first column), September (second column), and October (third column). Monthly-mean cloud fractions are also indicated. Stippling indicates significance at the 95% confidence levels of the trend. Ascension Island (8^0S, 14.5^0W) and St Helena Island (15^0S, 5^0W) are indicated by red and purple stars respectively.

5 Conclusions

By combining burned area data and meteorological reanalyses, we show early signs that the biomass burning season is starting later and is more intense in the middle of the fire season (August & September) with small fires likely contributing more over the 2003-2020 timespan. Regional differences in biomass burning suggest multiple drivers are contributing to the shift: internal displacement and local drying increasing fires in the Congo in June (Tyukavina et al., 2018; van Wees et al., 2021; Wimberly et al., 2024; Zhou et al., 2024), forestry management in Tanzania in July (Ract et al., 2024), and earlier prescribed burnings to reduce late season (October) wildfires in Zambia (Hollingsworth et al., 2015). If detection of small fires continues to improve, and if burning changes are robustly connected to current and projected precipitation shifts (Dunning et al., 2018; Attwood et al., 2024), then the trend of more small fires should persist across future datasets of burned area.

The changes in burning locations and timing in May-July do not significantly impact trends in fire emissions present over the southeast Atlantic (Figs. S6-S7), also consistent with the limited location of the increase in the weaker lower-level easterly winds that would account for the aerosol advection (Dobracki et al., 2024, Preprint). Instead, in August and September, more fires combine with increases in easterly free-tropospheric wind speeds to carry biomass burning aerosol further over the southeast Atlantic. A simple thermal wind analysis supports the deduction that land heating over Africa is a primary driver, coupled with a poleward expansion of the south Atlantic subtropical high (Vizy and Cook, 2016) that enhances the southern half of the SEA stratocumulus cloud deck. The exact mechanism behind the wind speed changes likely also includes other shifts in seasonal meteorological controls, such as from the mid-latitude westerly jets.

The changes in the AEJ-S also increase advection of warm free-tropospheric continental air over the ocean in September and October, at the southern edge of the stratocumulus deck. The increase in free-tropospheric stability (Fig. 9) will be further reinforced by increased shortwave absorption from the statistically-significant aerosol increase in September (Fig. 8b). Cloud fraction increases in these regions counterbalance cloud fraction decreases elsewhere (Fig. 9a-c). The combined increase in aerosol advection, along with a southward shift of the stratocumulus deck, explains the increase in the net direct aerosol radiative effect (a top-of-atmosphere cooling combined with an atmospheric warming from aerosol) noted by Jouan and Myrhe (2024) over the southeast Atlantic, and identifies September, a transition month, as the month experiencing the strongest changes. Statistically-significant aerosol-induced changes in cloud properties are otherwise not obvious, and impact on cloud structure

from a basin-wide increase in sea surface temperature must also be considered. Future work could perform mechanism denial experiments to better differentiate impacts on cloud properties from changing biomass burning emissions from those caused by large-scale circulation changes and sea surface temperature.

Declaration of competing interest

The authors declare that they have no known competing financial interests or personal relationships that could have appeared to influence the work reported in this paper.

CRediT authorship contribution statement

Tyler Tatro: Conceptualization, Methodology, Software, Investigation, Formal Analysis, Writing- Original Draft, Visualization. **Paquita Zuidema**: Conceptualization, Methodology, Writing- Review & Editing, Formal Analysis, Supervision, Validation

Acknowledgements

This work is supported by the Department of Energy Atmospheric System Research award DE-SC0021250 and by NASA award 80NSSC21K1344. GFED5 burned area data are available on https://zenodo.org/records/7668424. Fire_CCI and other burned area data from the ESA are available at https://climate.esa.int/en/projects/fire/data/. ERA5 and CAMS reanalysis are available through the ECMWF Copernicus data system. The Global Precipitation Climatology Project monthly analysis product is available from https://psl.noaa.gov/data/gridded/data.gpcp.html. Cloud droplet number concentration data are from https://catalogue.ceda.ac.uk/uuid/864a46cc65054008857ee5bb772a2a2b. CERES data can be obtained at https://ceres.larc.nasa.gov/data/. We thank the editor and the anonymous reviewers for comments that lead to improvements in the manuscript.

Appendix A. Supporting information for datasets

A1 Burned Area

The availability of satellite-derived burned area data products has grown in the last few decades, but the inability of these retrievals to accurately capture small fires (<1 km^2) significantly influences estimates of burned area, particularly in continental Africa (Roteta et al., 2019), where many fires are small, daytime-only, agricultural fires. These contrast to the 'mega-fires' of the northern hemisphere from the recent decade. In a study comparing high-resolution burned area (20 m) derived from the Sentinel-2 Multispectral Instrument against other 500-m resolution data products derived from MODIS, Ramo et al. (2021) found an 80% increase in burned area over Africa for 2016 when compared to burned area derived from Terra and Aqua MODIS sensors alone.

These differences impact trend estimates–previous literature based on 500m data suggests a decreasing trend in burned area during 2003-2017 in central southern Africa between 0-15°S (Jiang et al., 2020) and during 1997-2016 over 0-30°S (Andela et al., 2017), driven by less fires in savannas and grasslands. GFED5 corroborates declining fires in savannas and grasslands in the past 20 years, but the significance and magnitude of the burned area trend depends on the analyzed time period (Table 5 in Chen et al., 2023).

A2 Aerosol and Gas Reanalysis

CAMS CO and BC match the observed variability of the Ascension Island boundary layer well (Figure A1), but consistently underestimate CO and BC values under the smokiest conditions. The 500-700 hPa altitude captures the bulk of the lidar-derived aerosol vertical distribution from ORACLES measurements over the ocean (Redemann et al., 2021) in August through October, but the altitude of maximum CO concentration is lower (800 hPa) in May through July. CO_{LT} and CO_{MT} together contain ~76% of the total column CO over the continent (10°-40°W, 5°-20°S) and ~68% over the ocean (10°E-10°W, 5°-20°S) from May through October. CO_{LT} contains the majority of CO over the ocean in each month (~42%), although the true percentage is likely higher due to CAMS underestimating CO in the lower troposphere (Inness et al., 2022).

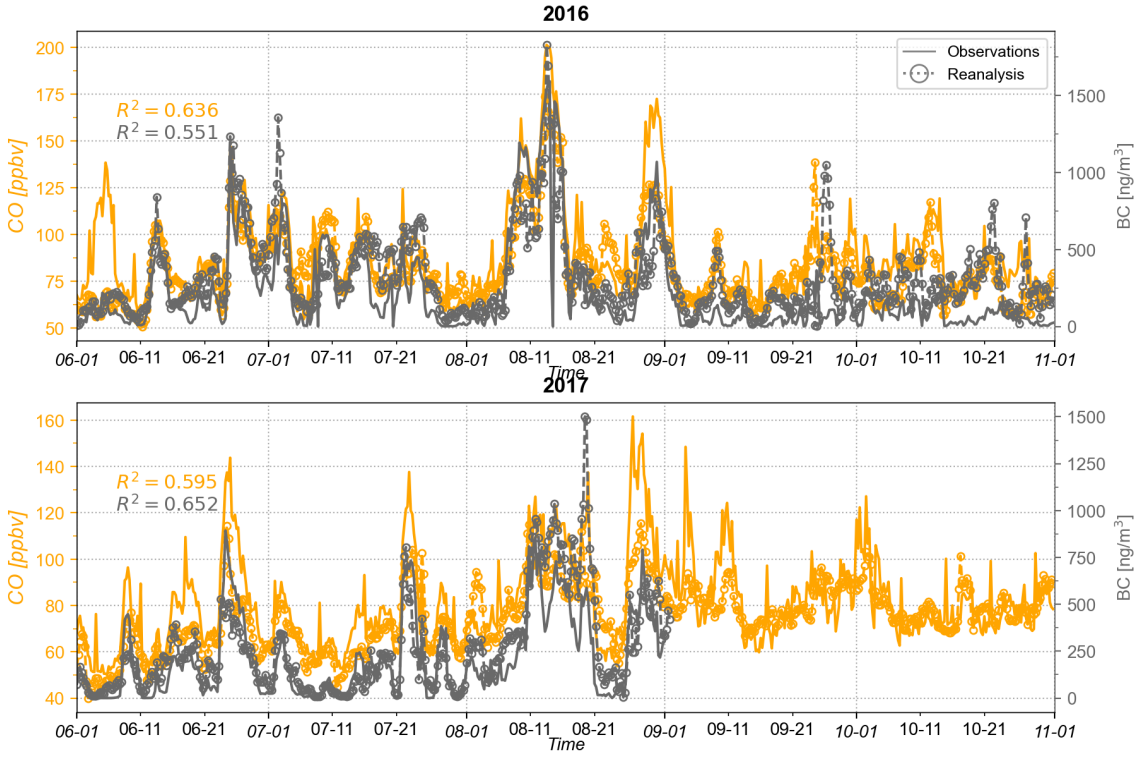

Figure A1. Comparison of CAMS CO and BC values at 960 hPa to LASIC observations at Ascension Island (8°S, 14.5°W) for June through October in 2016 (top panel) and 2017 (bottom panel). Note that LASIC BC measurements end on Aug 31, 2017.

CO levels have decreased globally from 2000 to 2020 caused by improvements in combustion technology (Novelli et al., 2003; Zheng et al., 2019; Buchholz et al., 2021). Therefore, we first isolate smoke transport changes over Africa from the background global reduction in CO. We estimate the global average CO column linear trend from the monthly anomalies averaged between 60°S to 60°N and over all longitudes, then subtract it from the monthly CO fields. We maintain the vertical partitioning of the reanalysis by adjusting the total column reduction so that it is proportional to the mass fraction of CO at each location, time, and altitude.

A3 Cloud Data

Two common products for examining changes in low cloud properties are the CERESCldTypHist_Ed4A product (used in this analysis) and the MODIS product (Pincus et al., 2023) used by JM24 and Wall et al., (2023). Both datasets use the 3.7 μm channel to retrieve liquid water path (LWP) and effective radius, but the two differ in

their treatment of partly cloudy (PCL) pixels (Minnis et al., 2011). CERES classifies pixels as cloudy or not (Minnis et al., 2008), while MODIS separates cloudy pixels into fully cloudy and partly cloudy (Platnick et al., 2017), often within scenes of broken clouds or at cloud edges. These pixels are provided with the MODIS dataset but are excluded from the cloud property analyses because three-dimensional radiative transfer effects will in the mean reduce the retrieved cloud optical depth and increase the retrieved cloud-top effective radius (r_e; Zuidema & Evans, 1998; Z. Zhang et al., 2016). The standard MODIS r_e retrieval, relied on here, uses the 2.1-micron channel. The Grosvenor et al., (2018) approach for constructing N_d, further reduces retrieval uncertainty by selecting, at the pixel level, for $r_e >$ 4 μm, a cloud optical depth greater than 4, a 5 km cloud fraction greater than 0.9, a solar zenith angle less than 65°, a satellite viewing zenith angle less than 55°, and a cloud mask sub-pixel homogeneity index less than 30. Of these criteria, the selection of optically-thicker, more horizontally expansive, cloud is most impactful for reducing the number of qualifying pixels. The pixel-level retrievals are then spatially aggregated into 1^0 boxes, with daily values made available through Gryspeerdt et al. (2022). For this paper, monthly averages of N_d are computed based on the daily-means. The N_d selection is not restricted further to the top 10% of the optically-thickest clouds. While this selection criterion is intended to help capture N_d values closer to the aerosol-activated values, the number of clouds sampled is also reduced, introducing another form of bias (Arola et al., 2022). In addition, a threshold for excluding precipitating clouds should be included simultaneously, one we lack. We also do not apply a specific ordering of the effective radius retrievals by wavelength, shown to have little impact on the N_d retrieval in Gryspeerdt et al., (2022) for the southeast Atlantic, perhaps because other error sources dominate. Inclusion of the r_e ordering criteria was found to produce higher N_d (not shown) while selecting for only the optically-thickest clouds was found to reduce the N_d, perhaps because of precipitation influences (also not shown, figures available upon request). Because this study focuses on N_d trends more than their absolute veracity, a choice was made to maintain a larger sample size for each month. The monthly means capture 50%-60% of the daily mean values over a 1^0 by 1^0 grid from August through October (Fig. A2), with a clear progression of higher N_d in August, reducing in September and October as less of the fire emissions enters the boundary layer (Fig. A3).

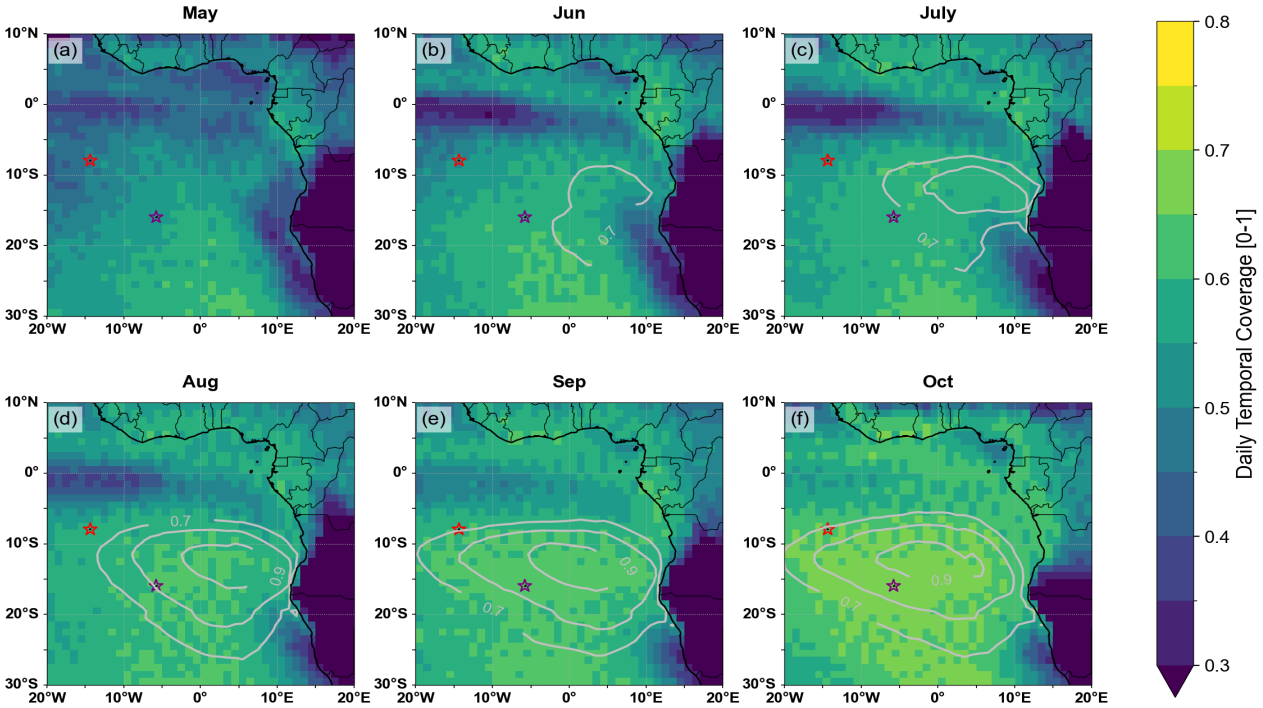

Figure A2. Temporal coverage (listed as a fraction of 1) of N_d_G18 in May through October.

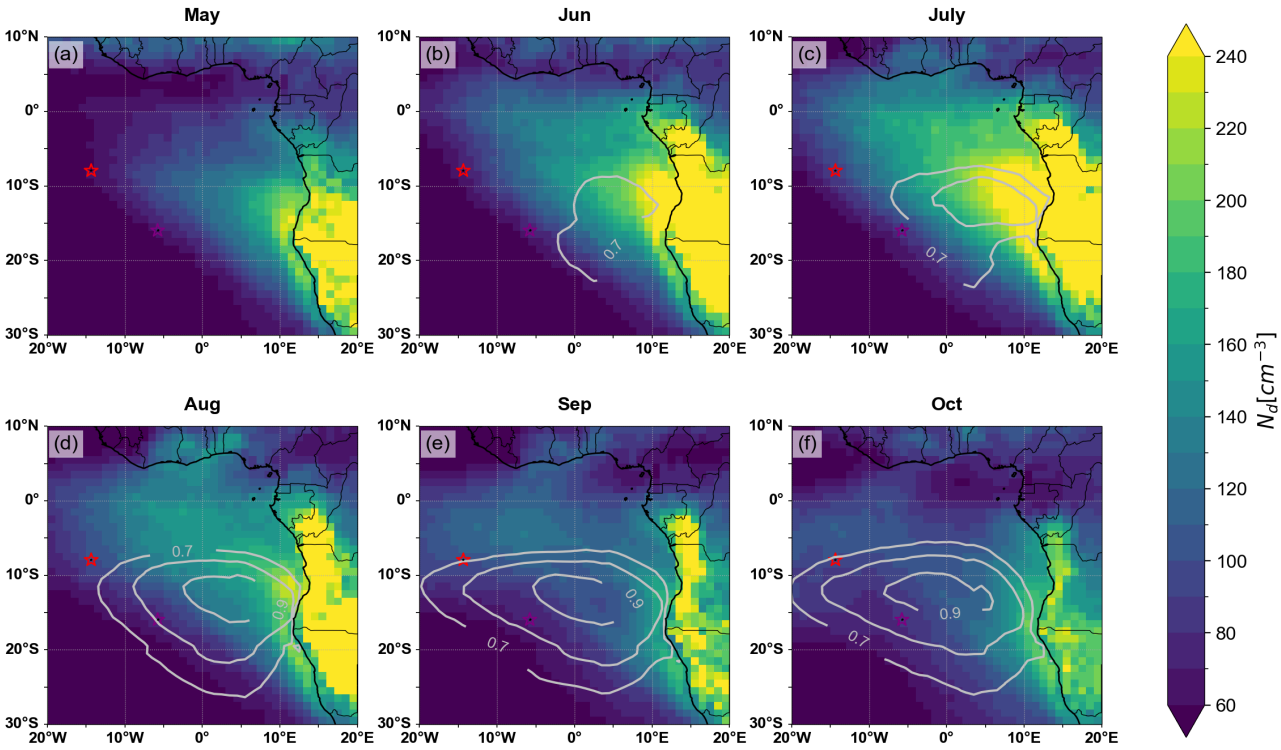

Figure A3. Seasonal cycle of N_d in May through October. Units of # per cm^{-3}. CERES LCF

Appendix B. Supplementary Information

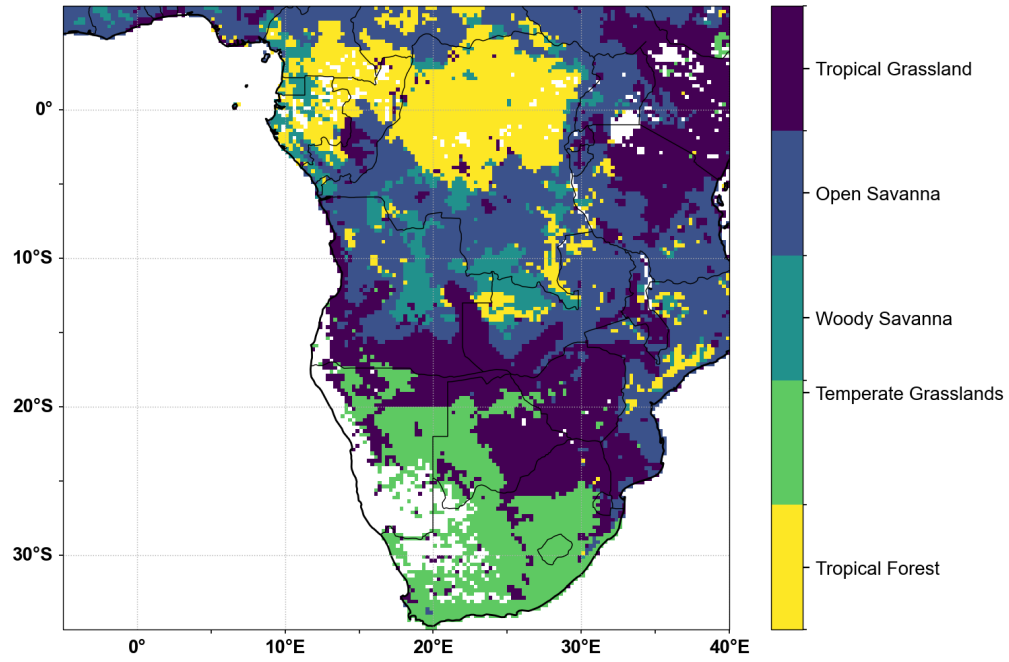

Figure S1. Map of vegetation types defined by GFED5 (modified IGBP scheme). Note that the land cover data used to generate GFED5 is on a 0.05° by 0.05° grid, but this plot shows the land cover type exhibiting the highest burned area average over the study period on 0.25°x0.25° resolution.

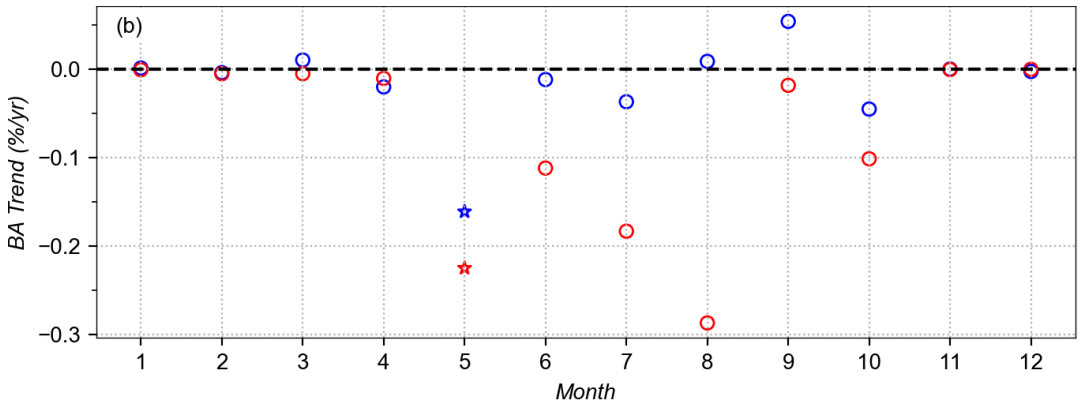

Figure S2. Difference in total burned area trends between GFED5 (blue circles) and Fire_CCI (red circles) normalized by the respective monthly average. Trends are averaged over 12-40°W and 0-30°S, for the period 2003-2020. The only trends significant at the 95% confidence level (marked as stars) are in May in both datasets.

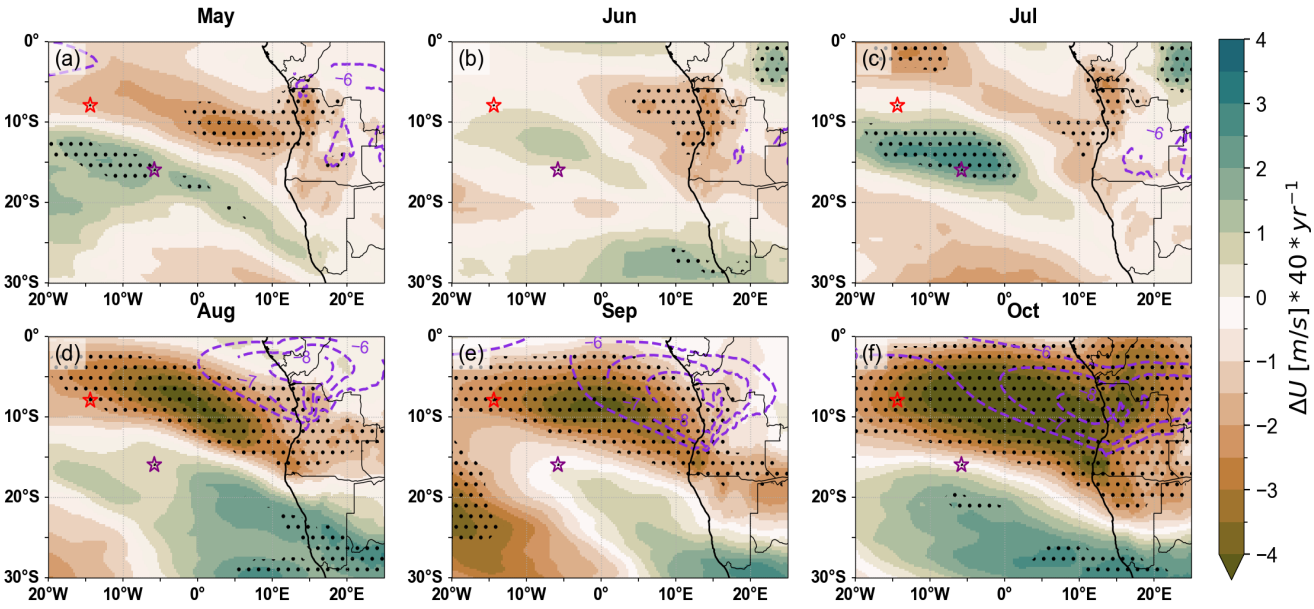

Figure S3. 1980-2020 Trend in ERA5 zonal wind (shading) at 800 hPa for May through July (a,b,c,) and at 700 hPa, 600 hPa, and 600 hPa for August (d), September (e), and October (f), respectively. Stippling indicates significance at the 95% confidence levels. Purple contours (-6, -7, -8 m/s) indicate the mean AEJ-S location in August through October. Ascension and St. Helena islands indicated (light and dark red stars).

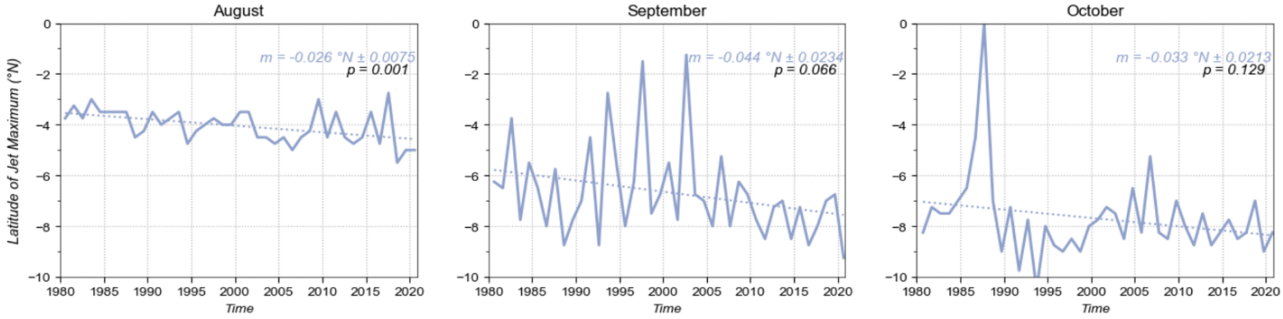

Figure S4. Time series of the latitude of AEJ-S maximum easterly wind speed (ERA5 minimum u-wind).

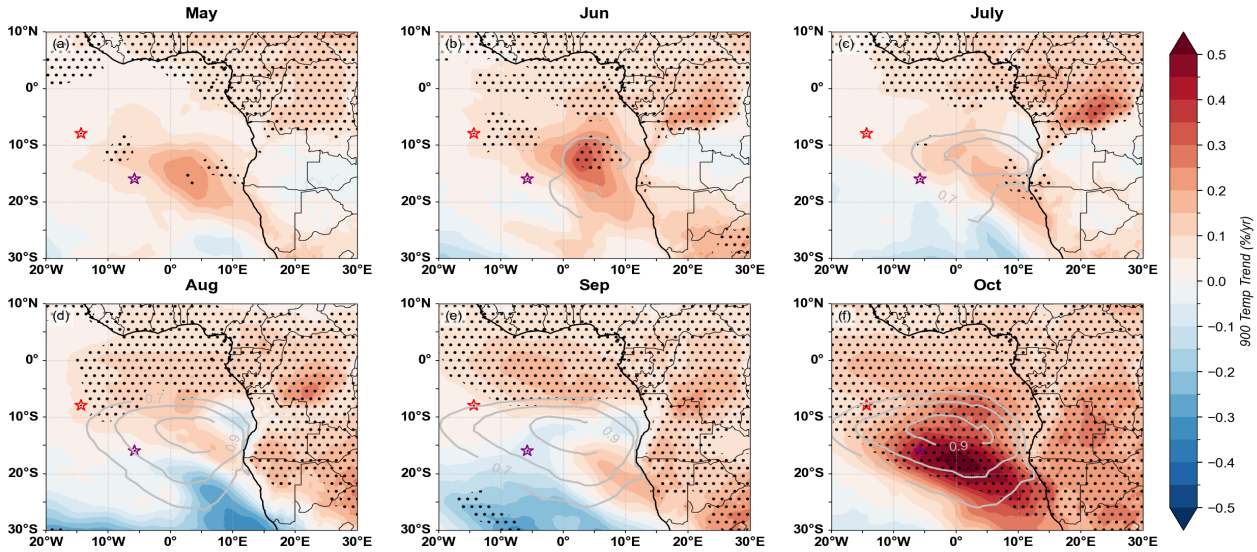

Figure S5. Trend in 900 hPa ERA5 temperature (shading) normalized by the monthly mean temperature, displayed with monthly mean cloud fraction (gray lines, 0.7-0.9). Stippling indicates significance at the 95% confidence levels.

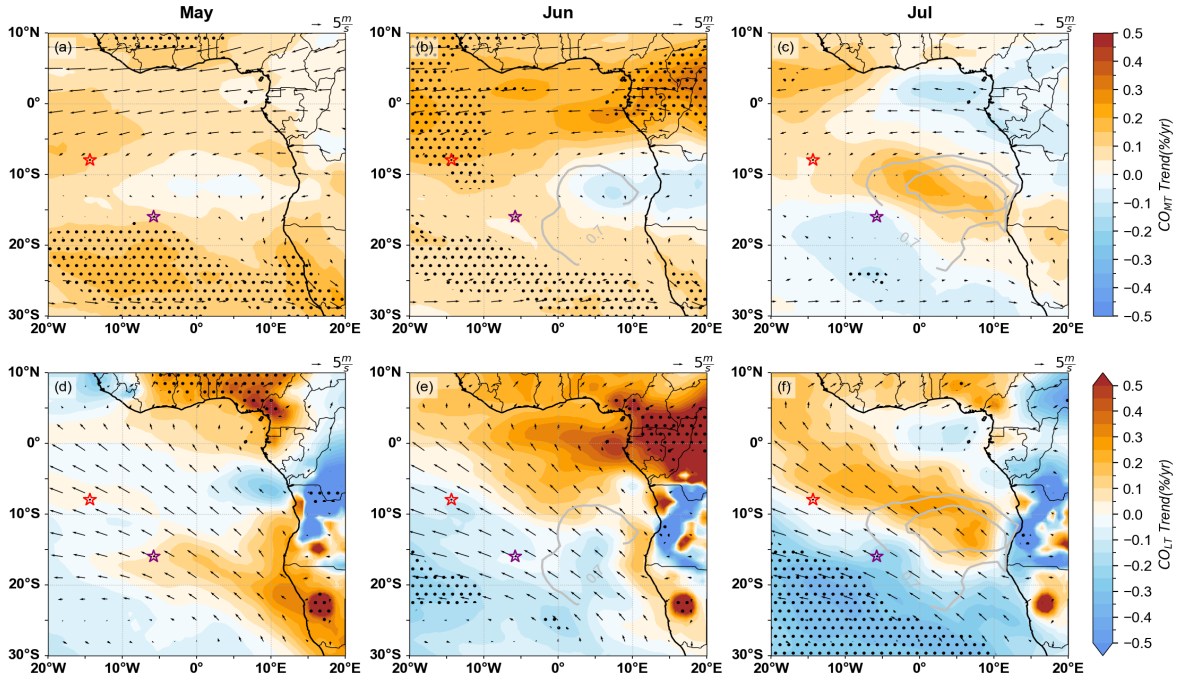

Figure S6. Residual trends in CO_{MT} (top row) and CO_{LT} (bottom row) for May to July (shaded) expressed as a percentage of the CO column mean, shown with mean circulation (vectors) at 700 hPa and 900 hPa, respectively, and mean low cloud fraction (gray contours, 0.7-0.9) for 2003-2022 (a-f). Stippling indicates significance of the regression line at the 95% confidence level.

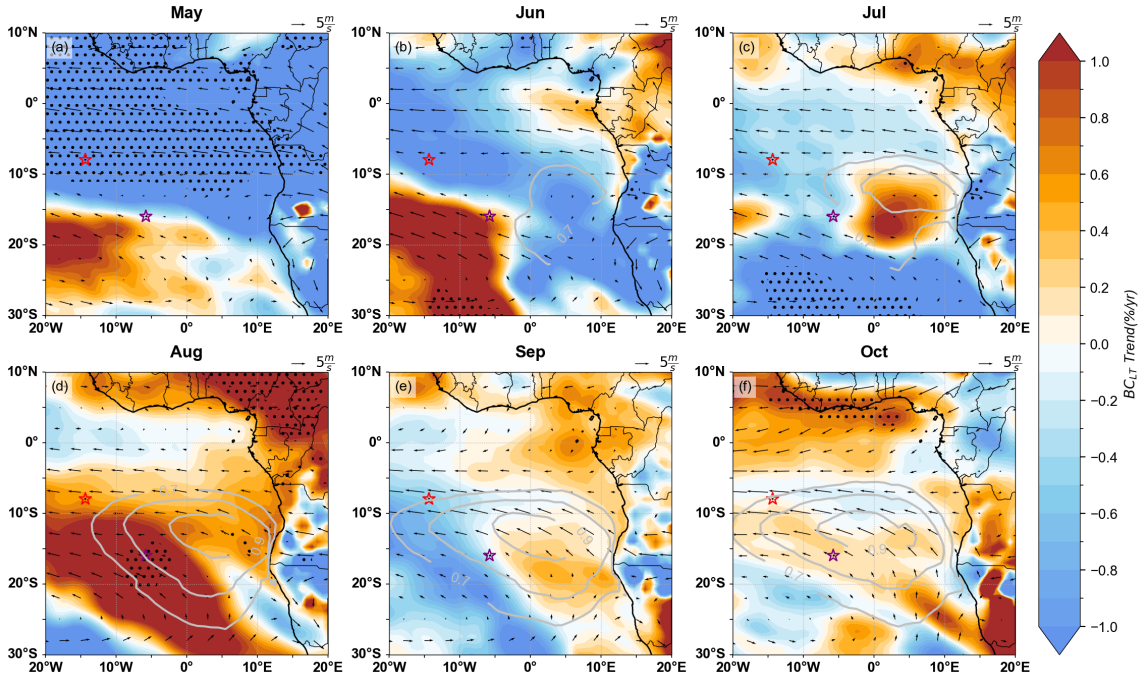

Figure S7. Trends in BC_{LT} for May to October (shaded) expressed as a percentage of the BC column mean, shown with mean circulation at 800 hPa (vectors) and mean low cloud fraction (gray contours, 0.7-0.9) for 2003-2022 (a-f). Stippling indicates significance of the regression line at the 95% confidence level.

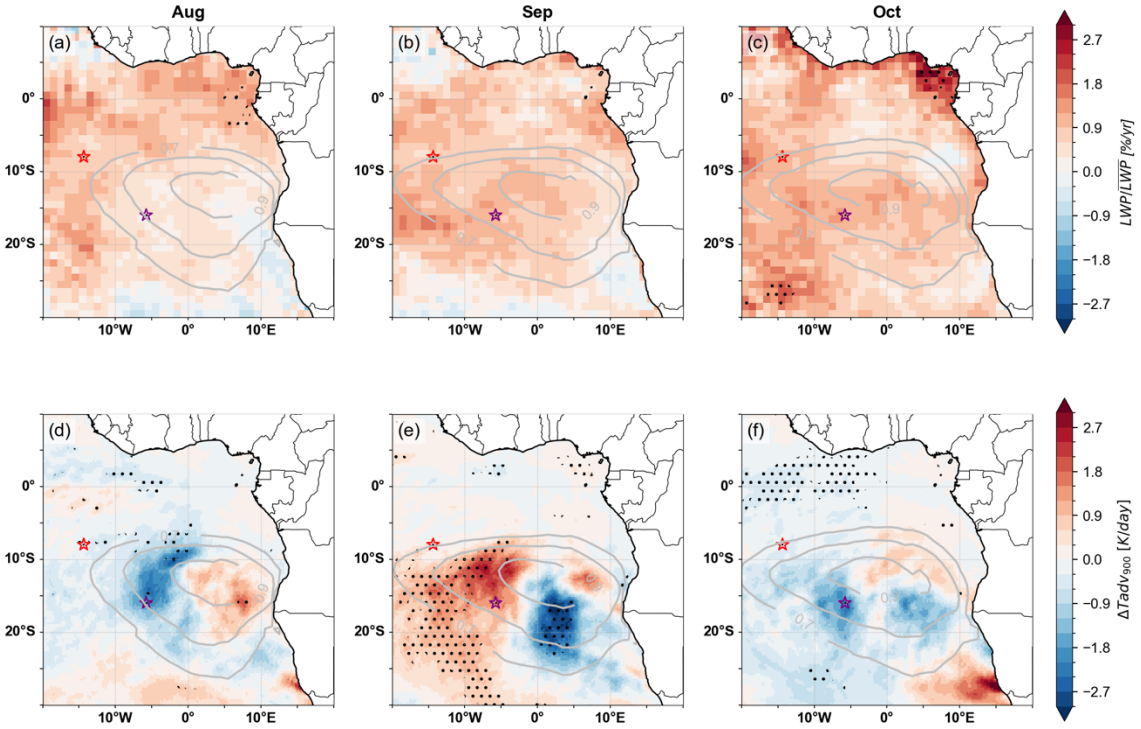

Figure S8. Trend in CERES liquid water path (top row) and ERA5 low-level (900 hPa) temperature advection (bottom row) for (a,d) August, (b,e) September, and (c,f) October. Stippling indicates significance of the regression line at the 95% confidence level.

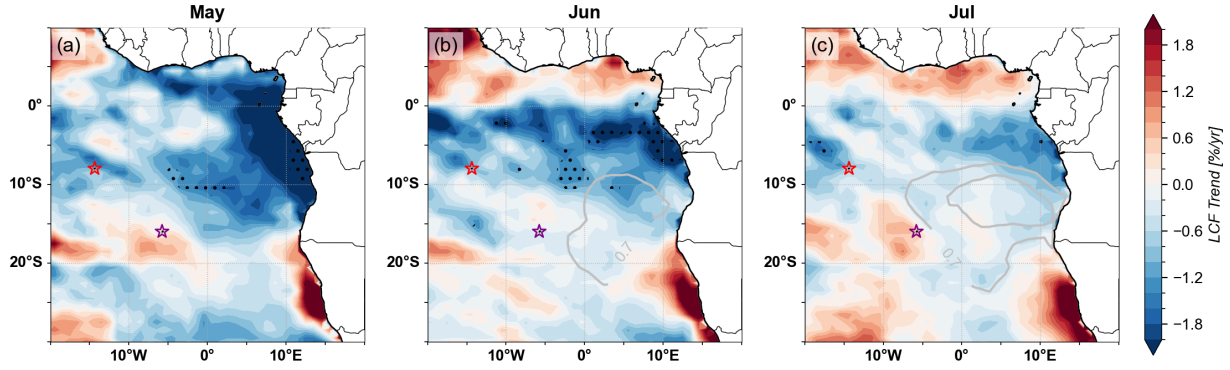

Figure S9. Trend in CERES low cloud fraction for a) May, b) June, and c) July. Stippling indicates significance of the regression line at the 95% confidence level.

References

Abel, S. J., Barrett, P. A., Zuidema, P., Zhang, J., Christensen, M., Peers, F., et al. (2020). Open cells exhibit weaker entrainment of free-tropospheric biomass burning aerosol into the south-east Atlantic boundary layer. *Atmospheric Chemistry and Physics*, *20*(7). https://doi.org/10.5194/acp-20-4059-2020

Ackerman, A. S., Toon, O. B., Stevens, D. E., Heymsfield, A. J., Ramanathan, V., & Welton, E. J. (2000). Reduction of tropical cloudiness by soot. *Science*, *288*(5468). https://doi.org/10.1126/science.288.5468.1042

Adebiyi, A. A., & Zuidema, P. (2016). The role of the southern African easterly jet in modifying the southeast Atlantic aerosol and cloud environments. *Quarterly Journal of the Royal Meteorological Society*, *142*(697). https://doi.org/10.1002/qj.2765

Adebiyi, A. A., & Zuidema, P. (2018). Low cloud cover sensitivity to biomass-burning aerosols and meteorology over the Southeast Atlantic. *Journal of Climate*, *31*(11). https://doi.org/10.1175/JCLI-D-17-0406.1

Andela, N., Morton, D. C., Giglio, L., Chen, Y., Van Der Werf, G. R., Kasibhatla, P. S., et al. (2017). A human-driven decline in global burned area. *Science*, *356*(6345). https://doi.org/10.1126/science.aal4108

Anyamba, A., Justice, C. O., Tucker, C. J., & Mahoney, R. (2003). Seasonal to interannual variability of vegetation and fires at SAFARI 2000 sites inferred from advanced very high resolution radiometer time series data. *Journal of Geophysical Research: Atmospheres*, *108*(13). https://doi.org/10.1029/2002jd002464

Arola, A., Lipponen, A., Kolmonen, P., Virtanen, T. H., Bellouin, N., Grosvenor, D. P., et al. (2022). Aerosol effects on clouds are concealed by natural cloud heterogeneity and satellite retrieval errors. *Nature Communications*, *13*(1). https://doi.org/10.1038/s41467-022-34948-5

Attwood, K., Washington, R., & Munday, C. (2024). The Southern African Heat Low: Structure, Seasonal and Diurnal Variability, and Climatological Trends. *Journal of Climate*. https://doi.org/10.1175/jcli-d-23-0522.1

Barkley, A. E., Prospero, J. M., Mahowald, N., Hamilton, D. S., Popendorf, K. J., Oehlert, A. M., et al. (2019). African biomass burning is a substantial source of phosphorus deposition to the Amazon, Tropical Atlantic Ocean, and Southern Ocean. *Proceedings of the National Academy of Sciences of the United States of America*, *116*(33). https://doi.org/10.1073/pnas.1906091116

Baró Pérez, A., Diamond, M. S., Bender, F. A. M., Devasthale, A., Schwarz, M., Savre, J., et al. (2024). Comparing the simulated influence of biomass burning plumes on low-level clouds over the southeastern Atlantic under varying smoke conditions. *Atmospheric Chemistry and Physics*, *24*(8), 4591–4610. https://doi.org/10.5194/acp-24-4591-2024

Bellomo, K., Clement, A. C., Mauritsen, T., Rädel, G., & Stevens, B. (2015). The influence of cloud feedbacks on equatorial atlantic variability. *Journal of Climate*, *28*(7). https://doi.org/10.1175/JCLI-D-14-00495.1

Boschetti, L., Roy, D. P., Giglio, L., Huang, H., Zubkova, M., & Humber, M. L. (2019). Global validation of the collection 6 MODIS burned area product. *Remote Sensing of Environment*, *235*. https://doi.org/10.1016/j.rse.2019.111490

Brandt, P., Bordbar, M. H., Coelho, P., Koungue, R. A. I., Körner, M., Lamont, T., et al. (2024). Physical Drivers of Southwest African Coastal Upwelling and Its Response to Climate Variability and Change. https://doi.org/10.1007/978-3-031-10948-5_9

Bretherton, C. S., Blossey, P. N., & Uchida, J. (2007). Cloud droplet sedimentation, entrainment efficiency, and subtropical stratocumulus albedo. *Geophysical Research Letters*, *34*(3). https://doi.org/10.1029/2006GL027648

Brown, H., Liu, X., Pokhrel, R., Murphy, S., Lu, Z., Saleh, R., et al. (2021). Biomass burning aerosols in most climate models are too absorbing. *Nature Communications*, *12*(1). https://doi.org/10.1038/s41467-020-20482-9

Buchholz, R. R., Worden, H. M., Park, M., Francis, G., Deeter, M. N., Edwards, D. P., et al. (2021). Air pollution trends measured from Terra: CO and AOD over industrial, fire-prone, and background regions. *Remote Sensing of Environment*, *256*. https://doi.org/10.1016/j.rse.2020.112275

Catarino, S., Romeiras, M. M., Figueira, R., Aubard, V., Silva, J. M. N., & Pereira, J. M. C. (2020). Spatial and temporal trends of burnt area in angola: Implications for natural vegetation and protected area management. *Diversity*, *12*(8). https://doi.org/10.3390/D12080307

Ceamanos, X., Coopman, Q., George, M., Riedi, J., Parrington, M., & Clerbaux, C. (2023). Remote sensing and model analysis of biomass burning smoke transported across the Atlantic during the 2020 Western US wildfire season. *Scientific Reports*, *13*(1). https://doi.org/10.1038/s41598-023-39312-1

Chen, Y., Hall, J., Van Wees, D., Andela, N., Hantson, S., Giglio, L., et al. (2023). Multi-decadal trends and variability in burned area from the 5th version of the Global Fire Emissions Database (GFED5). https://doi.org/10.5194/essd-2023-182

Christensen, M. W., Jones, W. K., & Stier, P. (2020). Aerosols enhance cloud lifetime and brightness along the stratus-to-cumulus transition. *Proceedings of the National Academy of Sciences of the United States of America*, *117*(30). https://doi.org/10.1073/pnas.1921231117

Das, S., Harshvardhan, H., Bian, H., Chin, M., Curci, G., Protonotariou, A. P., et al. (2017). Biomass burning aerosol transport and vertical distribution over the South African-Atlantic region. *Journal of Geophysical Research*, *122*(12). https://doi.org/10.1002/2016JD026421

Das, S., Colarco, P. R., & Harshvardhan, H. (2020). The Influence of Elevated Smoke Layers on Stratocumulus Clouds Over the SE Atlantic in the NASA Goddard Earth Observing System (GEOS) Model. *Journal of Geophysical Research: Atmospheres*, *125*(6). https://doi.org/10.1029/2019JD031209

Dedrick, J. L., Russell, L. M., Sedlacek, A. J., Kuang, C., Zawadowicz, M. A., & Lubin, D. (2024). Aerosol-Correlated Cloud Activation for Clean Conditions in the Tropical Atlantic Boundary Layer During LASIC. *Geophysical Research Letters*, *51*(3). https://doi.org/10.1029/2023GL105798

Deeter, M. N., Emmons, L. K., Francis, G. L., Edwards, D. P., Gille, J. C., Warner, J. X., et al. (2003). Operational carbon monoxide retrieval algorithm and selected results for the MOPITT instrument. *Journal of Geophysical Research: Atmospheres*, *108*(14). https://doi.org/10.1029/2002jd003186

Deeter, M. N., Edwards, D. P., Gille, J. C., & Drummond, J. R. (2007). Sensitivity of MOPITT observations to carbon monoxide in the lower troposphere. *Journal of Geophysical Research Atmospheres*, *112*(24). https://doi.org/10.1029/2007JD008929

Denjean, C., Bourrianne, T., Burnet, F., Mallet, M., Maury, N., Colomb, A., et al. (2020). Overview of aerosol optical properties over southern West Africa from DACCIWA aircraft measurements. *Atmospheric Chemistry and Physics*, *20*(8). https://doi.org/10.5194/acp-20-4735-2020

Diamond, M. S., Saide, P. E., Zuidema, P., Ackerman, A. S., Doherty, S. J., Fridlind, A. M., et al. (2022). Cloud adjustments from large-scale smoke-circulation interactions strongly modulate the southeastern Atlantic stratocumulus-to-cumulus transition. *Atmospheric Chemistry and Physics*, *22*(18). https://doi.org/10.5194/acp-22-12113-2022

Ding, S., & Liu, D. (2022). Evaluation of the CAMS reanalysis for atmospheric black carbon and carbon monoxide over the north China plain. *Environmental Pollution*, *314*. https://doi.org/10.1016/j.envpol.2022.120286

Dobracki, A., Lewis, E. R., Iii, A. J. S., Tatro, T., Zawadowicz, M. A., & Zuidema, P. (n.d.). Burning conditions and transportation pathways determine biomass-burning aerosol properties in the Ascension Island marine boundary layer. https://doi.org/10.5194/egusphere-2024-1347

Doherty, S. J., Saide, P. E., Zuidema, P., Shinozuka, Y., Ferrada, G. A., Gordon, H., et al. (2022). Modeled and observed properties related to the direct aerosol radiative effect of biomass burning aerosol over the southeastern Atlantic. *Atmospheric Chemistry and Physics*, *22*(1). https://doi.org/10.5194/acp-22-1-2022

Edwards, D. P., Emmons, L. K., Gille, J. C., Chu, A., Attié, J. L., Giglio, L., et al. (2006). Satellite-observed pollution from Southern Hemisphere biomass burning. *Journal of Geophysical Research Atmospheres*, *111*(14). https://doi.org/10.1029/2005JD006655

Field, R. D., Van Der Werf, G. R., Fanin, T., Fetzer, E. J., Fuller, R., Jethva, H., et al. (2016). Indonesian fire activity and smoke pollution in 2015 show persistent nonlinear sensitivity to El Niño-induced drought. *Proceedings of the National Academy of Sciences of the United States of America*, *113*(33). https://doi.org/10.1073/pnas.1524888113

Formenti, P., D'Anna, B., Flamant, C., Mallet, M., Piketh, S. J., Schepanski, K., et al. (2019). The aerosols, radiation and clouds in southern Africa field campaign in Namibia overview, illustrative observations, and way forward. *Bulletin of the American Meteorological Society*, *100*(7). https://doi.org/10.1175/BAMS-D-17-0278.1

Gareth, R., Roberts, G., Wooster, M. J., & Lagoudakis, E. (2009). Annual and diurnal african biomass burning temporal dynamics. *Biogeosciences*, *6*(5). https://doi.org/10.5194/bg-6-849-2009

Gelaro, R., McCarty, W., Suárez, M. J., Todling, R., Molod, A., Takacs, L., et al. (2017). The modern-era retrospective analysis for research and applications, version 2 (MERRA-2). *Journal of Climate*, *30*(14). https://doi.org/10.1175/JCLI-D-16-0758.1

Giglio, L., Descloitres, J., Justice, C. O., & Kaufman, Y. J. (2003). An enhanced contextual fire detection algorithm for MODIS. *Remote Sensing of Environment*, *87*(2–3). https://doi.org/10.1016/S0034-4257(03)00184-6

Giglio, L., Csiszar, I., & Justice, C. O. (2006). Global distribution and seasonality of active fires as observed with the Terra and Aqua Moderate Resolution Imaging Spectroradiometer (MODIS) sensors. *Journal of Geophysical Research: Biogeosciences*, *111*(2). https://doi.org/10.1029/2005JG000142

Giglio, L., Boschetti, L., Roy, D. P., Humber, M. L., & Justice, C. O. (2018). The Collection 6 MODIS burned area mapping algorithm and product. *Remote Sensing of Environment*, *217*. https://doi.org/10.1016/j.rse.2018.08.005

Gordon, H., Field, P. R., Abe, S. J., Dalvi, M., Grosvenor, D. P., Hill, A. A., et al. (2018). Large simulated radiative effects of smoke in the south-east Atlantic. *Atmospheric Chemistry and Physics*, *18*(20). https://doi.org/10.5194/acp-18-15261-2018

Griffin, D., Chen, J., Anderson, K., Makar, P., McLinden, C. A., Dammers, E., & Fogal, A. (2024). Biomass burning CO emissions: exploring insights through TROPOMI-derived emissions and emission coefficients. *Atmospheric Chemistry and Physics*, *24*(17), 10159–10186. https://doi.org/10.5194/acp-24-10159-2024

Grosvenor, D. P., Sourdeval, O., Zuidema, P., Ackerman, A., Alexandrov, M. D., Bennartz, R., et al. (2018). Remote Sensing of Droplet Number Concentration in Warm Clouds: A Review of the Current State of Knowledge and Perspectives. *Reviews of Geophysics*, *56*(2). https://doi.org/10.1029/2017RG000593

Gupta, G., Venkat Ratnam, M., Madhavan, B. L., & Narayanamurthy, C. S. (2022). Long-term trends in Aerosol Optical Depth obtained across the globe using multi-satellite measurements. *Atmospheric Environment*, *273*. https://doi.org/10.1016/j.atmosenv.2022.118953

Hall, J. V., Zibtsev, S. V., Giglio, L., Skakun, S., Myroniuk, V., Zhuravel, O., et al. (2021). Environmental and political implications of underestimated cropland burning in Ukraine. *Environmental Research Letters*, *16*(6). https://doi.org/10.1088/1748-9326/abfc04

Hansen, J., Sato, M., & Ruedy, R. (1997). Radiative forcing and climate response. *Journal of Geophysical Research Atmospheres*, *102*(D6). https://doi.org/10.1029/96JD03436

Haywood, J. M., Abel, S. J., Barrett, P. A., Bellouin, N., Blyth, A., Bower, K. N., et al. (2021). The CLoud-Aerosol-Radiation Interaction and Forcing: Year 2017 (CLARIFY-2017) measurement campaign. *Atmospheric Chemistry and Physics*, *21*(2). https://doi.org/10.5194/acp-21-1049-2021

Herbert, R. J., Bellouin, N., Highwood, E. J., & Hill, A. A. (2020). Diurnal cycle of the semi-direct effect from a persistent absorbing aerosol layer over marine stratocumulus in large-eddy simulations. *Atmospheric Chemistry and Physics*, *20*(3). https://doi.org/10.5194/acp-20-1317-2020

Hersbach, H., Bell, B., Berrisford, P., Hirahara, S., Horányi, A., Muñoz-Sabater, J., et al. (2020). The ERA5 global reanalysis. *Quarterly Journal of the Royal Meteorological Society*, *146*(730). https://doi.org/10.1002/qj.3803

Holanda, B. A., Pöhlker, M. L., Walter, D., Saturno, J., Sörgel, M., Ditas, J., et al. (2020). Influx of African biomass burning aerosol during the Amazonian dry season through layered transatlantic transport of black carbon-rich smoke. *Atmospheric Chemistry and Physics*, *20*(8). https://doi.org/10.5194/acp-20-4757-2020

Holloway, T., Levy, H., & Kasibhatla, P. (2000). Global distribution of carbon monoxide. *Journal of Geophysical Research Atmospheres*, *105*(D10). https://doi.org/10.1029/1999JD901173

Inness, A., Ades, M., Agustí-Panareda, A., Barr, J., Benedictow, A., Blechschmidt, A. M., et al. (2019). The CAMS reanalysis of atmospheric composition. *Atmospheric Chemistry and Physics*, *19*(6). https://doi.org/10.5194/acp-19-3515-2019

Inness, A., Aben, I., Ades, M., Borsdorff, T., Flemming, J., Jones, L., et al. (2022). Assimilation of S5P/TROPOMI carbon monoxide data with the global CAMS near-real-time system. *Atmospheric Chemistry and Physics*, *22*(21). https://doi.org/10.5194/acp-22-14355-2022

Jiang, Y., Zhou, L., & Raghavendra, A. (2020). Observed changes in fire patterns and possible drivers over Central Africa. *Environmental Research Letters*, *15*(9). https://doi.org/10.1088/1748-9326/ab9db2

Johansson, S., Wetzel, G., Friedl-Vallon, F., Glatthor, N., Höpfner, M., Kleinert, A., et al. (2022). Biomass burning pollution in the South Atlantic upper troposphere: GLORIA trace gas observations and evaluation of the CAMS model. *Atmospheric Chemistry and Physics*, *22*(5). https://doi.org/10.5194/acp-22-3675-2022

Johnson, B. T., & Haywood, J. M. (2023). Assessing the Impact of Self-Lofting on Increasing the Altitude of Black Carbon in a Global Climate Model. *Journal of Geophysical Research: Atmospheres*, *128*(8). https://doi.org/10.1029/2022JD038039

Johnson, B. T., Shine, K. P., & Forster, P. M. (2004). The semi-direct aerosol effect: Impact of absorbing aerosols on marine stratocumulus. *Quarterly Journal of the Royal Meteorological Society*, *130*(599 PART B). https://doi.org/10.1256/qj.03.61

Jouan, C., & Myhre, G. (2024). Satellite-based analysis of top of atmosphere shortwave radiative forcing trend induced by biomass burning aerosols over South-Eastern Atlantic. *Npj Climate and Atmospheric Science*, *7*(1). https://doi.org/10.1038/s41612-024-00631-3

Kacarab, M., Lee Thornhill, K., Dobracki, A., Howell, S. G., O'Brien, J. R., Freitag, S., et al. (2020). Biomass burning aerosol as a modulator of the droplet number in the southeast Atlantic region. *Atmospheric Chemistry and Physics*, *20*(5). https://doi.org/10.5194/acp-20-3029-2020

Kaiser, J. W., Heil, A., Andreae, M. O., Benedetti, A., Chubarova, N., Jones, L., et al. (2012). Biomass burning emissions estimated with a global fire assimilation system based on observed fire radiative power. *Biogeosciences*. https://doi.org/10.5194/bg-9-527-2012

Klein, S. A., & Hartmann, D. L. (1993). The seasonal cycle of low stratiform clouds. *Journal of Climate*, *6*(8). https://doi.org/10.1175/1520-0442(1993)006<1587:TSCOLS>2.0.CO;2

Korontzi, S. (2005). Seasonal patterns in biomass burning emissions from southern African vegetation fires for the year 2000. *Global Change Biology*, *11*(10). https://doi.org/10.1111/j.1365-2486.2005.001024.x

Kramer, R. J., He, H., Soden, B. J., Oreopoulos, L., Myhre, G., Forster, P. M., & Smith, C. J. (2021). Observational Evidence of Increasing Global Radiative Forcing. *Geophysical Research Letters*, *48*(7). https://doi.org/10.1029/2020GL091585

Kuete, G., Pokam Mba, W., & Washington, R. (2020). African Easterly Jet South: control, maintenance mechanisms and link with Southern subtropical waves. *Climate Dynamics*, *54*(3–4). https://doi.org/10.1007/s00382-019-05072-w

Kuete, G., Mba, W. P., James, R., Dyer, E., Annor, T., & Washington, R. (2023). How do coupled models represent the African Easterly Jets and their associated dynamics over Central Africa during the September–November rainy season? *Climate Dynamics*, *60*(9–10). https://doi.org/10.1007/s00382-022-06467-y

Liousse, C., Assamoi, E., Criqui, P., Granier, C., & Rosset, R. (2014). Explosive growth in African combustion emissions from 2005 to 2030. *Environmental Research Letters*, *9*(3). https://doi.org/10.1088/1748-9326/9/3/035003

Lizundia-Loiola, J., Otón, G., Ramo, R., & Chuvieco, E. (2020). A spatio-temporal active-fire clustering approach for global burned area mapping at 250 m from MODIS data. *Remote Sensing of Environment*, *236*. https://doi.org/10.1016/j.rse.2019.111493

Lou, S., Shrivastava, M., Easter, R. C., Yang, Y., Ma, P. L., Wang, H., et al. (2020). New SOA Treatments Within the Energy Exascale Earth System Model (E3SM): Strong Production and Sinks Govern Atmospheric SOA Distributions and Radiative Forcing. *Journal of Advances in Modeling Earth Systems*, *12*(12). https://doi.org/10.1029/2020MS002266

Lu, J., Vecchi, G. A., & Reichler, T. (2007). Expansion of the Hadley cell under global warming. *Geophysical Research Letters*, *34*(6). https://doi.org/10.1029/2006GL028443

Mallet, M., Nabat, P., Johnson, B., Michou, M., Haywood, J. M., Chen, C., & Dubovik, O. (2021). Climate models generally underrepresent the warming by central africa biomass-burning aerosols over the southeast atlantic. *Science Advances*, *7*(41). https://doi.org/10.1126/sciadv.abg9998

Manney, G. L., & Hegglin, M. I. (2018). Seasonal and regional variations of long-term changes in upper-tropospheric jets from reanalyses. *Journal of Climate*, *31*(1). https://doi.org/10.1175/JCLI-D-17-0303.1

Mehta, M., Singh, N., & Anshumali. (2018). Global trends of columnar and vertically distributed properties of aerosols with emphasis on dust, polluted dust and smoke - inferences from 10-year long CALIOP observations. *Remote Sensing of Environment*, *208*. https://doi.org/10.1016/j.rse.2018.02.017

Minnis, P., Trepte, Q. Z., Sun-Mack, S., Chen, Y., Doelling, D. R., Young, D. F., et al. (2008). Cloud detection in nonpolar regions for CERES using TRMM VIRS and Terra and Aqua MODIS data. *IEEE Transactions on Geoscience and Remote Sensing*, *46*(11), 3857–3884. https://doi.org/10.1109/TGRS.2008.2001351

Minnis, P., Sun-Mack, S., Young, D. F., Heck, P. W., Garber, D. P., Chen, Y., et al. (2011). CERES edition-2 cloud property retrievals using TRMM VIRS and Terra and Aqua MODIS data-Part I: Algorithms. *IEEE Transactions on Geoscience and Remote Sensing*, *49*(11 PART 2). https://doi.org/10.1109/TGRS.2011.2144601

Moriconi-Ebrard, F., Harre, D., & Heinrigs, P. (2016). *Urbanisation Dynamics in West Africa 1950–2010*. *OECD*.

Nicholson, S. E., & Grist, J. P. (2003). The seasonal evolution of the atmospheric circulation over West Africa and equatorial Africa. *Journal of Climate*, *16*(7). https://doi.org/10.1175/1520-0442(2003)016<1013:TSEOTA>2.0.CO;2

Novelli, P. C., Masarie, K. A., Lang, P. M., Hall, B. D., Myers, R. C., & Elkins, J. W. (2003). Reanalysis of tropospheric CO trends: Effects of the 1997-1998 wildfires. *Journal of Geophysical Research: Atmospheres*, *108*(15). https://doi.org/10.1029/2002jd003031

Pan, X., Ichoku, C., Chin, M., Bian, H., Darmenov, A., Colarco, P., et al. (2020). Six global biomass burning emission datasets: Intercomparison and application in one global aerosol model. *Atmospheric Chemistry and Physics*, *20*(2). https://doi.org/10.5194/acp-20-969-2020

Phiri, D., Mwitwa, J., Ng'andwe, P., Kanja, K., Munyaka, J., Chileshe, F., et al. (2023). Agricultural expansion into forest reserves in Zambia: a remote sensing approach. *Geocarto International*, *38*(1). https://doi.org/10.1080/10106049.2023.2213203

Pincus, R., Hubanks, P. A., Platnick, S., Meyer, K., Holz, R. E., Botambekov, D., & Wall, C. J. (2023). Updated observations of clouds by MODIS for global model assessment. *Earth System Science Data*, *15*(6). https://doi.org/10.5194/essd-15-2483-2023

Pistone, K., Wilcox, E. M., Zuidema, P., Giordano, M., Podolske, J., LeBlanc, S. E., et al. (2024). Vertical structure of a springtime smoky and humid troposphere over the southeast Atlantic from aircraft and reanalysis. *Atmospheric Chemistry and Physics*, *24*(13), 7983–8005. https://doi.org/10.5194/acp-24-7983-2024

Platnick, S., Meyer, K. G., King, M. D., Wind, G., Amarasinghe, N., Marchant, B., et al. (2017). The MODIS Cloud Optical and Microphysical Products: Collection 6 Updates and Examples from Terra and Aqua. *IEEE Transactions on Geoscience and Remote Sensing*, *55*(1). https://doi.org/10.1109/TGRS.2016.2610522

Ract, C., Burgess, N. D., Dinesen, L., Sumbi, P., Malugu, I., Latham, J., et al. (2024). Nature Forest Reserves in Tanzania and their importance for conservation. *PLoS ONE*, *19*(2 February). https://doi.org/10.1371/journal.pone.0281408

Rajapakshe, C., Zhang, Z., Yorks, J. E., Yu, H., Tan, Q., Meyer, K., et al. (2017). Seasonally transported aerosol layers over southeast Atlantic are closer to underlying clouds than previously reported. *Geophysical Research Letters*, *44*(11). https://doi.org/10.1002/2017GL073559

Ramo, R., Roteta, E., Bistinas, I., van Wees, D., Bastarrika, A., Chuvieco, E., & van der Werf, G. R. (2021). African burned area and fire carbon emissions are strongly impacted by small fires undetected by coarse resolution satellite data. *Proceedings of the National Academy of Sciences of the United States of America*, *118*(9). https://doi.org/10.1073/pnas.2011160118

Redemann, J., Wood, R., Zuidema, P., Doherty, S. J., Luna, B., LeBlanc, S. E., et al. (2021, February 4). An overview of the ORACLES (ObseRvations of aerosols above CLouds and their intEractionS) project: Aerosol-cloud-radiation interactions in the southeast Atlantic basin. *Atmospheric Chemistry and Physics*. Copernicus GmbH. https://doi.org/10.5194/acp-21-1507-2021

Roteta, E., Bastarrika, A., Padilla, M., Storm, T., & Chuvieco, E. (2019). Development of a Sentinel-2 burned area algorithm: Generation of a small fire database for sub-Saharan Africa. *Remote Sensing of Environment*, *222*. https://doi.org/10.1016/j.rse.2018.12.011

Ryoo, J. M., Pfister, L., Ueyama, R., Zuidema, P., Wood, R., Chang, I., & Redemann, J. (2021). A meteorological overview of the ORACLES (ObseRvations of Aerosols above CLouds and their intEractionS) campaign over the southeastern Atlantic during 2016-2018: Part 1 - Climatology. *Atmospheric Chemistry and Physics*, *21*(22). https://doi.org/10.5194/acp-21-16689-2021

Schutgens, N., Tsyro, S., Gryspeerdt, E., Goto, D., Weigum, N., Schulz, M., & Stier, P. (2017). On the spatio-temporal representativeness of observations. *Atmospheric Chemistry and Physics*, *17*(16). https://doi.org/10.5194/acp-17-9761-2017

Scott, R. C., Myers, T. A., Norris, J. R., Zelinka, M. D., Klein, S. A., Sun, M., & Doelling, D. R. (2020). Observed sensitivity of low-cloud radiative effects to meteorological perturbations over the global oceans. *Journal of Climate*, *33*(18). https://doi.org/10.1175/JCLI-D-19-1028.1

Seethala, C., Norris, J. R., & Myers, T. A. (2015). How has subtropical stratocumulus and associated meteorology changed since the 1980s? *Journal of Climate*, *28*(21). https://doi.org/10.1175/JCLI-D-15-0120.1

Shinozuka, Y., Kacenelenbogen, M. S., Burton, S. P., Howell, S. G., Zuidema, P., Ferrare, R. A., et al. (2020). Daytime aerosol optical depth above low-level clouds is similar to that in adjacent clear skies at the same heights: Airborne observation above the southeast Atlantic. *Atmospheric Chemistry and Physics*, *20*(19). https://doi.org/10.5194/acp-20-11275-2020

Shinozuka, Y., Saide, P. E., Ferrada, G. A., Burton, S. P., Ferrare, R., Doherty, S. J., et al. (2020). Modeling the smoky troposphere of the southeast Atlantic: A comparison to ORACLES airborne observations from September of 2016. *Atmospheric Chemistry and Physics*, *20*(19). https://doi.org/10.5194/acp-20-11491-2020

Sun, X., Cook, K. H., & Vizy, E. K. (2017). The South Atlantic subtropical high: Climatology and interannual variability. *Journal of Climate*, *30*(9). https://doi.org/10.1175/JCLI-D-16-0705.1

Twomey, S. (1977). The Influence of Pollution on the Shortwave Albedo of Clouds. *Journal of the Atmospheric Sciences*, *34*(7). https://doi.org/10.1175/1520-0469(1977)034<1149:tiopot>2.0.co;2

Tyukavina, A., Hansen, M. C., Potapov, P., Parker, D., Okpa, C., Stehman, S. V., et al. (2018). Congo Basin forest loss dominated by increasing smallholder clearing. *Science Advances*, *4*(11). https://doi.org/10.1126/sciadv.aat2993

United Nations High Commissioner for Refugees. (2023). *Angola Registration Report 2023*. Retrieved from https://data.unhcr.org/en/documents/details/100903

van der Velde, I. R., van der Werf, G. R., van Wees, D., Schutgens, N. A. J., Vernooij, R., Houweling, S., et al. (2024). Small Fires, Big Impact: Evaluating Fire Emission Estimates in Southern Africa Using New Satellite Imagery of Burned Area and Carbon Monoxide. *Geophysical Research Letters*, *51*(12). https://doi.org/10.1029/2023GL106122

Vizy, E. K., & Cook, K. H. (2016). Understanding long-term (1982–2013) multi-decadal change in the equatorial and subtropical South Atlantic climate. *Climate Dynamics*, *46*(7–8). https://doi.org/10.1007/s00382-015-2691-1

Wall, C. J., Storelvmo, T., & Possner, A. (2023). Global observations of aerosol indirect effects from marine liquid clouds. *Atmospheric Chemistry and Physics*, *23*(20). https://doi.org/10.5194/acp-23-13125-2023

Ward, D. E., Hao, W. M., Susott, R. A., Babbitt, R. E., Shea, R. W., Kauffman, J. B., & Justice, C. O. (1996). Effect of fuel composition on combustion efficiency and emission factors for African savanna ecosystems. *Journal of Geophysical Research Atmospheres*, *101*(19). https://doi.org/10.1029/95jd02595

van Wees, D., van der Werf, G. R., Randerson, J. T., Andela, N., Chen, Y., & Morton, D. C. (2021). The role of fire in global forest loss dynamics. *Global Change Biology*, *27*(11). https://doi.org/10.1111/gcb.15591

Van Wees, D., Van Der Werf, G. R., Randerson, J. T., Rogers, B. M., Chen, Y., Veraverbeke, S., et al. (2022). Global biomass burning fuel consumption and emissions at 500 m spatial resolution based on the Global Fire Emissions Database (GFED). *Geoscientific Model Development*, *15*(22). https://doi.org/10.5194/gmd-15-8411-2022

Wen, G., Marshak, A., Cahalan, R. F., Remer, L. A., & Kleidman, R. G. (2007). 3-D aerosol-cloud radiative interaction observed in collocated MODIS and ASTER images of cumulus cloud fields. *Journal of Geophysical Research Atmospheres*, *112*(13). https://doi.org/10.1029/2006JD008267

Van Der Werf, G. R., Randerson, J. T., Giglio, L., Collatz, G. J., Kasibhatla, P. S., & Arellano, A. F. (2006). Interannual variability in global biomass burning emissions from 1997 to 2004. *Atmospheric Chemistry and Physics*, *6*(11). https://doi.org/10.5194/acp-6-3423-2006

Van Der Werf, G. R., Randerson, J. T., Giglio, L., Collatz, G. J., Mu, M., Kasibhatla, P. S., et al. (2010). Global fire emissions and the contribution of deforestation, savanna, forest, agricultural, and peat fires (1997-2009). *Atmospheric Chemistry and Physics*, *10*(23). https://doi.org/10.5194/acp-10-11707-2010

Wiedinmyer, C., Kimura, Y., Mcdonald-Buller, E. C., Emmons, L. K., Buchholz, R. R., Tang, W., et al. (2023). The Fire Inventory from NCAR version 2.5: an updated global fire emissions model for climate and chemistry applications. *Geoscientific Model Development*, *16*(13). https://doi.org/10.5194/gmd-16-3873-2023

Wielicki, B. A., Barkstrom, B. R., Harrison, E. F., Lee, R. B., Smith, G. L., & Cooper, J. E. (1996). Clouds and the Earth's Radiant Energy System (CERES): An Earth Observing System Experiment. *Bulletin of the American Meteorological Society*, *77*(5). https://doi.org/10.1175/1520-0477(1996)077<0853:CATERE>2.0.CO;2

van Wilgen, B. W., Everson, C. S., & Trollope, W. S. W. (1990). Fire Management in Southern Africa: Some Examples of Current Objectives, Practices, and Problems. https://doi.org/10.1007/978-3-642-75395-4_11

Wimberly, M. C., Wanyama, D., Doughty, R., Peiro, H., & Crowell, S. (2024). Increasing Fire Activity in African Tropical Forests Is Associated With Deforestation and Climate Change. *Geophysical Research Letters*, *51*(9). https://doi.org/10.1029/2023GL106240

Winker, D. M., Vaughan, M. A., Omar, A., Hu, Y., Powell, K. A., Liu, Z., et al. (2009). Overview of the CALIPSO mission and CALIOP data processing algorithms. *Journal of Atmospheric and Oceanic Technology*, *26*(11). https://doi.org/10.1175/2009JTECHA1281.1

Wood, R., & Bretherton, C. S. (2006). On the relationship between stratiform low cloud cover and lower-tropospheric stability. *Journal of Climate*, *19*(24). https://doi.org/10.1175/JCLI3988.1

Woollings, T., Drouard, M., O'Reilly, C. H., Sexton, D. M. H., & McSweeney, C. (2023). Trends in the atmospheric jet streams are emerging in observations and could be linked to tropical warming. *Communications Earth and Environment*, *4*(1). https://doi.org/10.1038/s43247-023-00792-8

Wu, H., Taylor, J. W., Szpek, K., Langridge, J. M., Williams, P. I., Flynn, M., et al. (2020). Vertical variability of the properties of highly aged biomass burning aerosol transported over the southeast Atlantic during CLARIFY-2017. *Atmospheric Chemistry and Physics*, *20*(21). https://doi.org/10.5194/acp-20-12697-2020

Yurganov, L., McMillan, W., Grechko, E., & Dzhola, A. (2010). Analysis of global and regional co burdens measured from space between 2000 and 2009 and validated by ground-based solar tracking spectrometers. *Atmospheric Chemistry and Physics*, *10*(8). https://doi.org/10.5194/acp-10-3479-2010

Zhang, J., & Feingold, G. (2023). Distinct regional meteorological influences on low-cloud albedo susceptibility over global marine stratocumulus regions. *Atmospheric Chemistry and Physics*, *23*(2). https://doi.org/10.5194/acp-23-1073-2023

Zhang, J., & Zuidema, P. (2019). The diurnal cycle of the smoky marine boundary layer observed during August in the remote southeast Atlantic. *Atmospheric Chemistry and Physics*, *19*(23). https://doi.org/10.5194/acp-19-14493-2019

Zhang, J., & Zuidema, P. (2021). Sunlight-absorbing aerosol amplifies the seasonal cycle in low-cloud fraction over the southeast Atlantic. *Atmospheric Chemistry and Physics*, *21*(14). https://doi.org/10.5194/acp-21-11179-2021

Zhang, Z., Werner, F., Cho, H. M., Wind, G., Platnick, S., Ackerman, A. S., et al. (2016). A framework based on 2-D Taylor expansion for quantifying the impacts of subpixel reflectance variance and covariance on cloud optical thickness and effective radius retrievals based on the bispectral method. *Journal of Geophysical Research*, *121*(12). https://doi.org/10.1002/2016JD024837

Zheng, B., Chevallier, F., Ciais, P., Yin, Y., & Wang, Y. (2018). On the Role of the Flaming to Smoldering Transition in the Seasonal Cycle of African Fire Emissions. *Geophysical Research Letters*, *45*(21). https://doi.org/10.1029/2018GL079092

Zheng, B., Chevallier, F., Yin, Y., Ciais, P., Fortems-Cheiney, A., Deeter, M. N., et al. (2019). Global atmospheric carbon monoxide budget 2000-2017 inferred from multi-species atmospheric inversions. *Earth System Science Data*, *11*(3). https://doi.org/10.5194/essd-11-1411-2019

Zuidema, P., & Evans, K. F. (1998). On the validity of the independent pixel approximation for boundary layer clouds observed during ASTEX. *Journal of Geophysical Research Atmospheres*, *103*(D6). https://doi.org/10.1029/98JD00080

Zuidema, P., Chang, P., Medeiros, B., Kirtman, B. P., Mechoso, R., Schneider, E. K., et al. (2016). Challenges and prospects for reducing coupled climate model sst biases in the eastern tropical atlantic and pacific oceans: The U.S. Clivar eastern tropical oceans synthesis working group. *Bulletin of the American Meteorological Society*, *97*(12). https://doi.org/10.1175/BAMS-D-15-00274.1

Zuidema, P., Sedlacek, A. J., Flynn, C., Springston, S., Delgadillo, R., Zhang, J., et al. (2018). The Ascension Island Boundary Layer in the Remote Southeast Atlantic is Often Smoky. *Geophysical Research Letters*, *45*(9). https://doi.org/10.1002/2017GL076926